Article

PEO-CYTOP Fluoropolymer Nanosheets as a Novel Open-Skull Window for Imaging of the Living Mouse Brain

Suppression of bleeding

2 mm

in vivo Ca²⁺ imaging in vast FOV

2 mm

PEO-CYTOP nanosheet

Skull

Brain tissue

PEO PEO PEO PEO PEO PEO

CYTOP

thickness: 130 nm

in vivo deep imaging with natural curvature of brain surface

1 mm

Taiga Takahashi, Hong Zhang, Ryosuke Kawakami, ..., Kohei Otomo, Yosuke Okamura, Tomomi Nemoto

tn@nips.ac.jp

HIGHLIGHTS

PEO-CYTOP nanosheet enables *in vivo* deep brain imaging in a vast field of view

The 130 nm thickness and the hydrophilized surface realize the strong adhesiveness

Suppressions of bleeding from the surface and inflammation in long-term are achieved

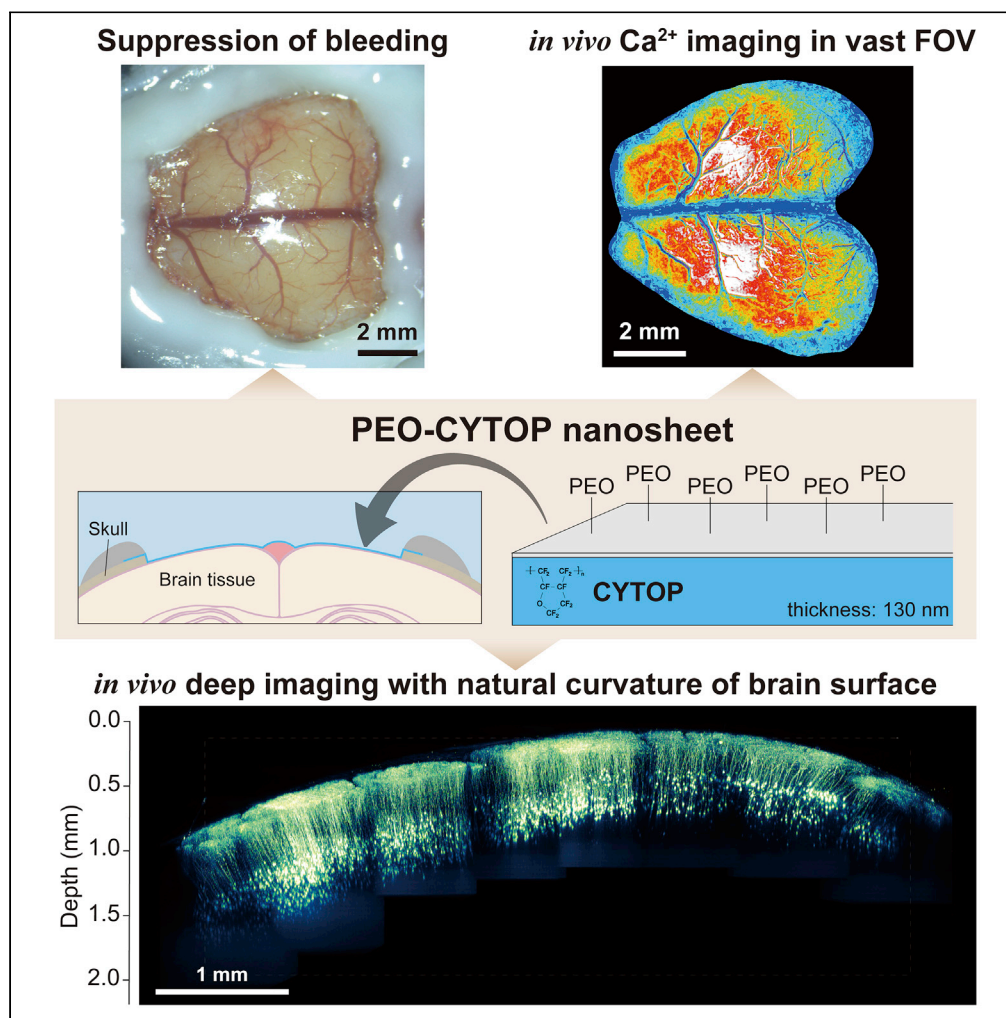The vast and transparent cranial window with natural curvature of the surface

Article

PEO-CYTOP Fluoropolymer Nanosheets as a Novel Open-Skull Window for Imaging of the Living Mouse Brain

Taiga Takahashi,[1,2,3,4,5] Hong Zhang,[6,7] Ryosuke Kawakami,[4,5,8] Kenji Yarinome,[9] Masakazu Agetsuma,[10] Junichi Nabekura,[3,10] Kohei Otomo,[1,2,3,4,5] Yosuke Okamura,[6,7,9] and Tomomi Nemoto[1,2,3,4,5,11,*]

SUMMARY

In vivo two-photon deep imaging with a broad field of view has revealed functional connectivity among brain regions. Here, we developed a novel observation method that utilizes a polyethylene-oxide-coated CYTOP (PEO-CYTOP) nanosheet with a thickness of ∼130 nm that exhibited a water retention effect and a hydrophilized adhesive surface. PEO-CYTOP nanosheets firmly adhered to brain surfaces, which suppressed bleeding from superficial veins. By taking advantage of the excellent optical properties of PEO-CYTOP nanosheets, we performed *in vivo* deep imaging in mouse brains at high resolution. Moreover, PEO-CYTOP nanosheets enabled to prepare large cranial windows, achieving *in vivo* imaging of neural structure and Ca^{2+} elevation in a large field of view. Furthermore, the PEO-CYTOP nanosheets functioned as a sealing material, even after the removal of the dura. These results indicate that this method would be suitable for the investigation of neural functions that are composed of interactions among multiple regions.

INTRODUCTION

Multiple regional measurements in the living brains of animals have been used to clarify the anatomical and functional connectivity between brain regions and their underlying functions (Sporns et al., 2005; Okano et al., 2016). Functional magnetic resonance imaging and magnetoencephalography have been employed to identify brain networks in mesoscale; however, these methods did not provide observation of local neural circuits at the subcellular level. In contrast, *in vivo* two-photon fluorescence microscopy visualizes neural activities and ensembles at subcellular resolution in living mammalian brains across multiple regions (Theer et al., 2003; Kondo et al., 2017; Ebina et al., 2018). This microscopic technique is used especially in deeper regions of the living brain because the near-infrared laser light pulses employed for two-photon excitation are less scattered and absorbed than is the excitation laser light in the visible range that is usually employed in confocal microscopy (Denk et al., 1990; Helmchen and Denk, 2005; Nemoto et al., 2015).

For deep imaging of living mouse brains using two-photon fluorescence microscopy, most researchers employ the "open skull method," in which the cranial hole that is employed for observation is usually sealed with a glass coverslip (Holtmaat et al., 2009; Goldey et al., 2014). The surgical operation that is used to achieve a cranial window without injury of the brain surface or bleeding is difficult because of the necessary removal of the submillimeter-thick cranial skull. Notably, it is more challenging to achieve cranial windows in the regions located near or under the superior sagittal sinus, including the prefrontal cortex (PFC), because the sinus cavities bleed easily and re-bleeding occurs frequently. In turn, the bleeding on the surface of the brain deteriorates fluorescent signals and optically accessible depth because of the optical absorption of hemoglobin. Moreover, the regrowth and thickening of the dura frequently occurs in long-term observations, thus deteriorating the optical transparency of chronic cranial windows. In addition, the size of cranial windows sealed with a glass coverslip has been usually restricted to 6 mm in diameter, at maximum. Recently, researchers have proposed novel methods for enlarging the field of view (FOV), such as curved-glass or soft-polymer windows (Heo et al., 2016; Kim et al., 2016; Ghanbari et al., 2019) and optical clearing techniques of the skull (Zhao et al., 2018; Zhang et al., 2018a). However, these methods utilize thick sealing materials with a high refractive index, resulting in various optical aberrations.

[1]Biophotonics Research Group, Exploratory Research Center on Life and Living Systems (ExCELLS), National Institutes of Natural Sciences, Higashiyama 5-1, Myodaiji, Okazaki, Aichi 444-8787, Japan

[2]Division of Biophotonics, National Institute for Physiological Sciences, National Institutes of Natural Sciences, Higashiyama 5-1, Myodaiji, Okazaki, Aichi 444-8787, Japan

[3]School of Life Science, The Graduate University for Advanced Studies (SOKENDAI), Higashiyama 5-1, Myodaiji, Okazaki, Aichi 444-8787, Japan

[4]Research Institute for Electronic Science, Hokkaido University, Hokkaido, Kita 20 Nishi 10, Kita-ku, Sapporo, Hokkaido 001-0020, Japan

[5]Graduate School of Information Science and Technology Hokkaido University, Hokkaido, Kita 20 Nishi 10, Kita-ku, Sapporo, Hokkaido 001-0020, Japan

[6]Department of Applied Chemistry, School of Engineering, Tokai University, 4-1-1 Kitakaname, Hiratsuka, Kanagawa 259-1292, Japan

[7]Micro/Nano Technology Center, Tokai University, 4-1-1 Kitakaname, Hiratsuka, Kanagawa 259-1292, Japan

[8]Department of Molecular Medicine for Pathogenesis, Graduate School of Medicine Ehime University, Shitsukawa 454, Toon, Ehime 791-0295, Japan

[9]Course of Applied Science, Graduate School of Engineering, Tokai University, 4-1-1 Kitakaname, Hiratsuka, Kanagawa 259-1292, Japan

Continued

In the field of biomaterials, polymer thin films with a thickness in the order of 10–100 nm, which are known as nanosheets, have been proposed as novel materials for surgical application (Okamura et al., 2009, 2013; Fujie et al., 2010; Hagisawa et al., 2013; Komachi et al., 2017) and bioimaging (Zhang et al., 2017, 2018b; Someya et al., 2018). Nanosheets have unique properties, including high adhesion strength, flexibility, and transparency. In particular, nanosheets with a thickness of 200 nm or less have strong physical absorption on the object surface (Okamura et al., 2009; Fujie et al., 2010). Recently, biocompatible nanosheets were developed to stop bleeding effectively without harmful effects under postoperative conditions (Hagisawa et al., 2013; Komachi et al., 2017). As a bioimaging application, a fluoropolymer nanosheet with a high water retention effect has been found to facilitate the long-term observation of cleared fixed-mouse-brain slices with a larger area (Zhang et al., 2017).

In this study, we developed a novel fluoropolymer nanosheet called "polyethylene-oxide-coated CYTOP (PEO-CYTOP) nanosheet," in which a single-side surface was hydrophilized by PEO. Using this nanosheet as a sealing material in the open-skull method, instead of a glass coverslip, we were able to implement a larger cranial window with a size that was approximately equal to that of the parietal region. Using this window, we performed *in vivo* two-photon imaging of neural structures, as well as time-lapse *in vivo* imaging of Ca^{2+} elevation. Finally, we carried out long-term imaging of the Ca^{2+} transients and of neural structures without the dura using the PEO-CYTOP nanosheet.

RESULTS

PEO-CYTOP Nanosheet with a Water Retention Effect and a Hydrophilized Adhesive Surface

The amorphous perfluoro (1-butenyl vinyl ether) polymer, commercially known as CYTOP, was chosen as the material to constitute the nanosheet in this study. The fabrication process is shown in Figure 1A in schematic form. By employing poly(vinyl alcohol) (PVA) to form a sacrificial layer, the nanosheet could be lifted out of water and transferred to any other surface. Because of the inert nature of CYTOP, direct chemical grafting on CYTOP was difficult. Thus, we applied a layer of polydimethylsiloxane (PDMS) with a thickness of ∼7 nm onto the CYTOP nanosheet (Figure S1A).

After exposure to oxygen plasma, the treated side of the nanosheet became more hydrophilic, as hydroxyl groups were introduced. Moreover, the hydrophilic silane reagent trichlorosilane termination PEO-silane was then applied for coupling with the hydroxyl groups, so that a stabilized hydrophilic surface was obtained on CYTOP (Figure S1B). A surface element analysis of the nanosheet was then performed using X-ray photoelectron spectroscopy, which indicated the validity of each step of the surface modification (Figure S1C). Moreover, the PEO-CYTOP nanosheet had approximately 100% transmittance in the wavelength range of 300–800 nm, indicating its optical transparency and suitability for *in vivo* imaging (Figure S1D).

After immersion in water, the PEO-CYTOP nanosheet floated on its surface as the underlying PVA layer dissolved (Figure 1B). For adherence of the nanosheet to the mouse brain, a nonwoven fabric was then applied as a transfer substrate, to support the nanosheet keeping the hydrophilic side facing outward, as shown in Figure 1C. The contact angle results verified the hetero-surface property of the PEO-CYTOP nanosheet, in which we were able to distinguish both the hydrophobicity and hydrophilicity on the two sides of the nanosheet (Figure 1D). The morphology of the nanosheet was then observed using scanning electron microscopy, which confirmed that the surface of the nanosheet was flat and uniform and devoid of any cracks or wrinkles (Figure 1E). In a practical imaging task, the hydrophilic side of the PEO-CYTOP nanosheet came into contact with the mouse brain to improve its interfacial adhesion capability. In this study, we developed an evaluation method, as shown in the scheme presented in Figure 1F. Magnetic nanoparticles-loaded hydrogel was fabricated as a tissue model and placed on the surface of the nanosheet, which was then placed in close proximity to a magnet. We found that the distance of dragging of the hydrogel on the CYTOP and PEO-CYTOP nanosheet was ∼6.7 and ∼2.8 mm, respectively (Figure 1G). Assuming that the strength of the magnetic field on a symmetry axis in the pole direction falls off as the inverse square of the distance, the maximum friction that the PEO-CYTOP nanosheet could provide was almost 80 times larger than that of the CYTOP nanosheet (Zhang et al., 2017). This result indicated that the PEO-CYTOP nanosheet could restrict sliding between the tissue and the nanosheet. The water retention effect was another feature of nanosheet wrapping; this effect was evaluated using a method reported previously (Zhang et al., 2017). In this process, the water in the hydrogel evaporated at room temperature, and the water retention ratio was calculated from the weight loss (Figure 1H). Without the nanosheet, the hydrogel became

[10]Division of Homeostatic Development, National Institute for Physiological Sciences, National Institutes of Natural Sciences, Okazaki, 444-8585, Japan

[11]Lead Contact

*Correspondence:
tn@nips.ac.jp
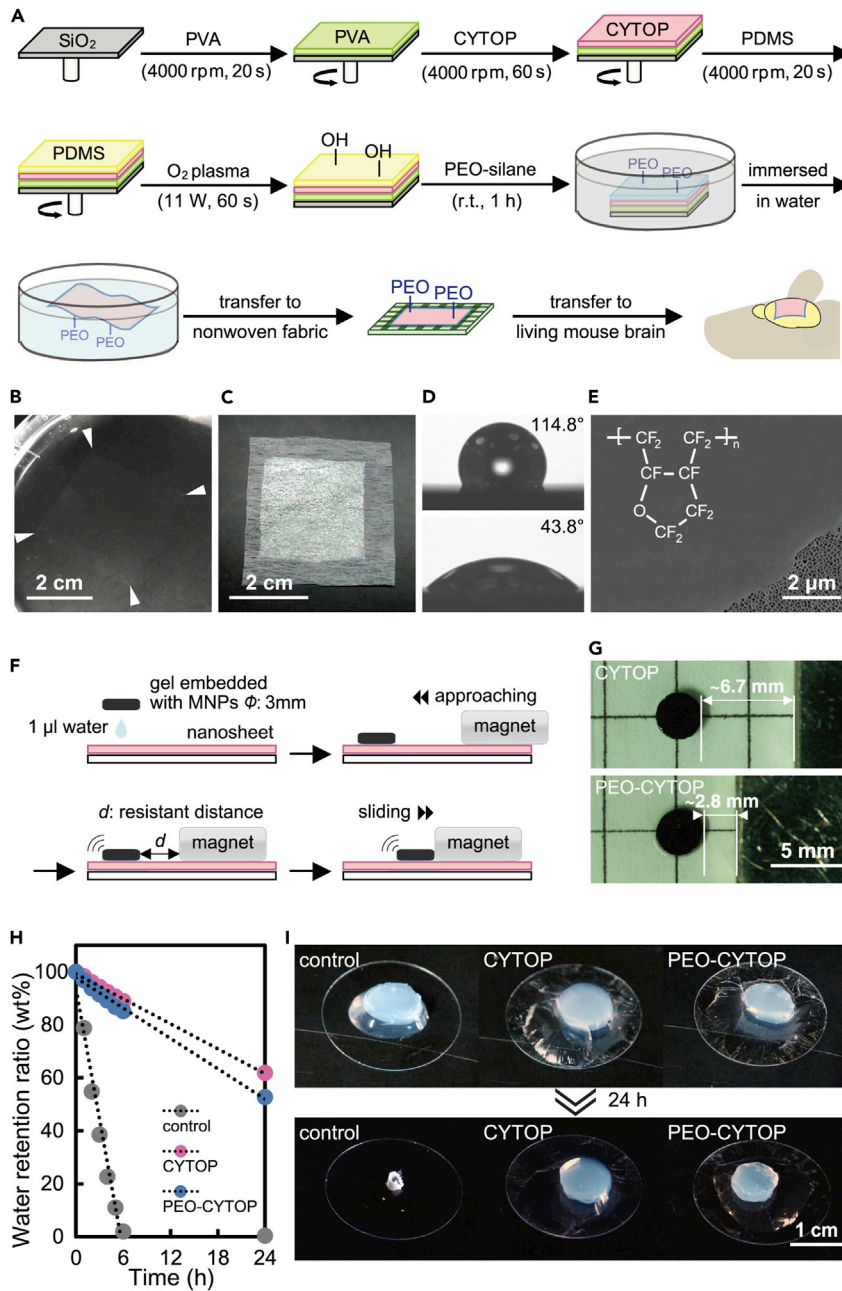
Figure 1. Fabrication and Characterization of the PEO-CYTOP Nanosheet

(A) Schematic representation of the fabrication of a freestanding PEO-CYTOP nanosheet re-supported on a nonwoven fabric for wrapping the living mouse brain.

(B) Image of a PEO-CYTOP nanosheet with a thickness of ~130 nm floating on the surface of the water (the arrows indicate the corner of the nanosheet).

(C) Image of an ~130-nm PEO-CYTOP nanosheet re-supported on a nonwoven fabric with the hydrophilic side facing outward.

(D) Static water contact angle of the hydrophobic and hydrophilic sides of the PEO-CYTOP nanosheet.

(E) Scanning electron micrograph of a PEO-CYTOP nanosheet adhered onto an Anodisc membrane.

(F) Schematic representation showing the evaluation of the adhesion capability of the nanosheet using a magnet-driven method.

(G) Images captured at the moment at which an magnetic nanoparticle-loaded hydrogel overcomes the maximum friction, to be dragged over the CYTOP and PEO-CYTOP nanosheets.

Figure 1. *Continued*
(H) Correlation between the water retention ratio and the time of the test using the CYTOP and PEO-CYTOP nanosheet-wrapped hydrogels.
(I) Photographs of the hydrogels wrapped with the CYTOP and PEO-CYTOP nanosheets (without nanosheet wrapping as a control) after 24 h.

completely dehydrated within 6 h. However, when a hydrogel was wrapped around a ∼130-nm CYTOP nanosheet, the evaporation was primarily prevented and ∼60 wt % of water was retained, even after 24 h (Figure 1I). This trend was also confirmed in the PEO-CYTOP nanosheet, which retained ∼50 wt % of the water. Thus, we concluded that the hydrophilic surface modification performed in this study yields no significant degradation in terms of the water retention effect, suggesting that the living mouse brain can be observed over a long time.

PEO-CYTOP Nanosheet as a Viable Material for the Establishment of Cranial Windows

We examined whether the PEO-CYTOP nanosheet could be used to seal a cranial window spanning the whole parietal region of a mouse brain (Figure 2A). First, we removed the skull and cleaned the fragments of the skull, as reported previously (Holtmaat et al., 2009; Goldey et al., 2014). Next, a PEO-CYTOP nanosheet supported by a nonwoven fabric was placed onto the brain surface, with the hydrophilic side of the PEO-CYTOP nanosheet facing the brain surface (Figures 2B and 2C). In addition, we carefully touched the PEO-CYTOP nanosheet via the nonwoven fabric, to transfer the nanosheet from the nonwoven fabric to the brain surface. The nonwoven fabric was removed after confirming that the nanosheet was transferred to the brain surface (Figure 2E). Because of the stronger adhesion of the hydrophilic adhesive surface, the nanosheet adhered to the brain surface without glue. To verify the effect of bleeding suppression, we demonstrated that the PEO-CYTOP nanosheet suppressed bleeding from superficially wounded veins by injuring the right transverse sinus intentionally after attaching a PEO-CYTOP nanosheet (Figure S2). In the case of bleeding occurring from the sinus, the blood did not spread over the initial points to the rostral regions beneath the PEO-CYTOP nanosheet. After the resealing of a bleeding, re-bleeding did not occur from the injured sinus. The effect of suppressed bleeding from superficial brain veins afforded by the PEO-CYTOP nanosheet served to keep the cranial window clean and devoid of blood coagulation (Figure S3).

Moreover, the higher flexibility of the PEO-CYTOP nanosheet enabled the establishment of a larger cranial window that conventional glass coverslips would not be able to seal. The area of this window (Figure 2E) was over 50 mm^2 from the top. Therefore, this vast cranial hole covering almost the entire surface of the parietal region was sealed entirely with PEO-CYTOP nanosheet.

In Vivo Two-Photon Imaging of Neural Morphology Using the PEO-CYTOP Nanosheet

To confirm that the cranial windows afforded by the PEO-CYTOP nanosheet were compatible with *in vivo* mouse brain imaging, we conducted *in vivo* two-photon imaging in Thy1-EYFP-H mice (Feng et al., 2000) (Figures 3A–3F). We acquired several series of fluorescence images of the living mouse brain crossing the superior sagittal sinus vertically (over 3 mm in length), as shown in Figure 3B, and in parallel (over 6 mm in length), as shown in Figure 3C. Under these conditions, we obtained fluorescence images at a subcellular resolution (Figures 3D–3F). The curvature of the brain shown in Figures 3B and 3C and Video S1 indicated that the brain surface was not distorted. The axons and the dendrites were visualized in cross-sectional *xy*-images of EYFP fluorescence (Figure 3D). The pyramidal neurons were visualized at a deeper layer, up to a depth of 700 μm, corresponding to layer 6 of the primary visual cortex (Figures 3E and 3F).

To evaluate the optical properties of the PEO-CYTOP nanosheets and glass coverslips, we measured point spread functions (PSFs) by obtaining fluorescence images of 200-nm yellow-green beads embedded with an agarose gel (Figure S4). The lateral full width at half maximum (FWHM) of PSF through PEO-CYTOP was 436 ± 1.67 nm (mean ± standard error, n = 10), and that recorded through glass coverslips was 437 ± 2.05 nm. There was no significant difference in the lateral FWHM of PSFs between the two materials (Figure S4E). Conversely, the axial FWHM of PSF through PEO-CYTOP was 1.68 ± 0.03 μm and that of glass coverslips was 1.99 ± 0.02 μm, i.e., compared with the glass coverslips, the axial FWHM of PSF through PEO-CYTOP was significantly narrower. Moreover, we sequentially performed *in vivo* two-photon imaging of the PFC through an identical cranial window, which was first sealed with the PEO-CYTOP nanosheet followed by resealing with a coverslip after removing the nanosheet (Figure S5, see Transparent Methods). Compared with images obtained via both cranial windows, although the PEO-CYTOP nanosheet did not
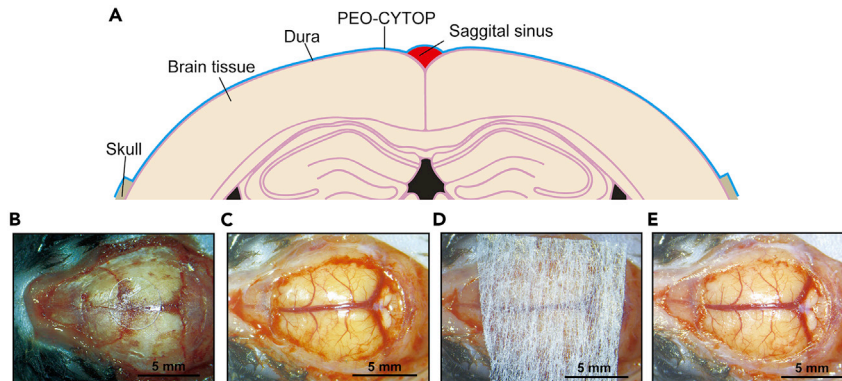
Figure 2. Application of the PEO-CYTOP Nanosheet to the Cranial Window for *In Vivo* Two-Photon Imaging

(A) Schematic drawing of the cranial window covered by the PEO-CYTOP nanosheet.

(B) Skull view after removal of the hair and scalp and placement of a glass coverslip with a diameter of 4.2 mm.

(C) Exposure of the brain tissues after removal of the cranial skull, with preservation of the dura.

(D) The PEO-CYTOP nanosheet on the nonwoven fabric was placed on the brain surface.

(E) Cranial window with the PEO-CYTOP nanosheet.

improve the imaging quality, the structures of the soma or those of the dendritic branches achieved were not prominently different, even in the deep layers. Thus, we ensured that the PEO-CYTOP nanosheet could be used for *in vivo* two-photon imaging as a covering material of the cranial window, and that it did not deteriorate the neural structure in deep and wide-field imaging.

We also assessed the stability of the FOV against the motion artifact under anesthesia and awake conditions (Figure S6). We observed astrocytes stained by sulforhodamine 101 through a window with a diameter of 4.2 mm that was sealed with a glass coverslip or a PEO-CYTOP nanosheet, and a window with a diameter of >8 mm that was sealed with a PEO-CYTOP nanosheet. We evaluated the correlation coefficient between the reference frame and each frame (see Transparent Methods). As depicted in Figures S6A–S6D, the glass coverslip suppressed the displacement of the FOV because it pressed the brain tissue tightly. In the case of the PEO-CYTOP nanosheet, although we did not completely suppress the displacement resulting from respiratory and fatal movements, the natural curvature of the brain surface was maintained.

Wide-Field *In Vivo* Imaging of Ca^{2+} Transient Using the PEO-CYTOP Nanosheet

To evaluate the effects of PEO-CYTOP nanosheets on neural activities, we next carried out *in vivo* Ca^{2+} imaging in G7NG817 transgenic mice, which express a genetically encoded Ca^{2+} indicator protein, GCaMP7, in a varying proportion of neurons and astrocytes (Monai et al., 2016). As shown in Figure 4A, Ca^{2+} elevations were observed at low magnification by epifluorescence microscopy through a large cranial window that was sealed with the PEO-CYTOP nanosheet. By stimulating the G7NG817 mouse by intermittent tail pinching, significant fluorescent transient Ca^{2+} elevations were also observed in multiple regions (Figures 4B and 4C). Thus, we confirmed that the PEO-CYTOP nanosheet afforded *in vivo* imaging of Ca^{2+} elevations with a larger FOV.

Chronic *In Vivo* Two-Photon Imaging Combining a PEO-CYTOP Nanosheet with a Glass Coverslip

To confirm that the PEO-CYTOP nanosheet is not harmful to the living mouse neural activities during longitudinal observations, we performed *in vivo* two-photon Ca^{2+} imaging in an identical G7NG817 mouse for 4–9 weeks after surgery. We placed a glass coverslip on the cranial window sealed with a PEO-CYTOP nanosheet, to protect against mouse behaviors, including scratching (Figures 5A and 5B). We found that the brain tissue without any sealing materials resulted in edema and bleeding from the brain tissue (Figure S7). At 4–9 weeks after surgery, the transparency of the cranial window was maintained successfully, at a level of 87.5% (14 out of 16). We also visualized cells at a depth of ~150 μm from GCaMP7 signals, for long-term imaging (Figures 5C–5E). Noticeably, we found that the PEO-CYTOP nanosheet significantly inhibited the regrowth of the dura and bleeding. Thus, astrocytes were successfully observed up to a depth of 230 ± 59 μm (mean $\pm$ standard error, n = 4 animals) at 4 weeks after surgery. In addition, we represented
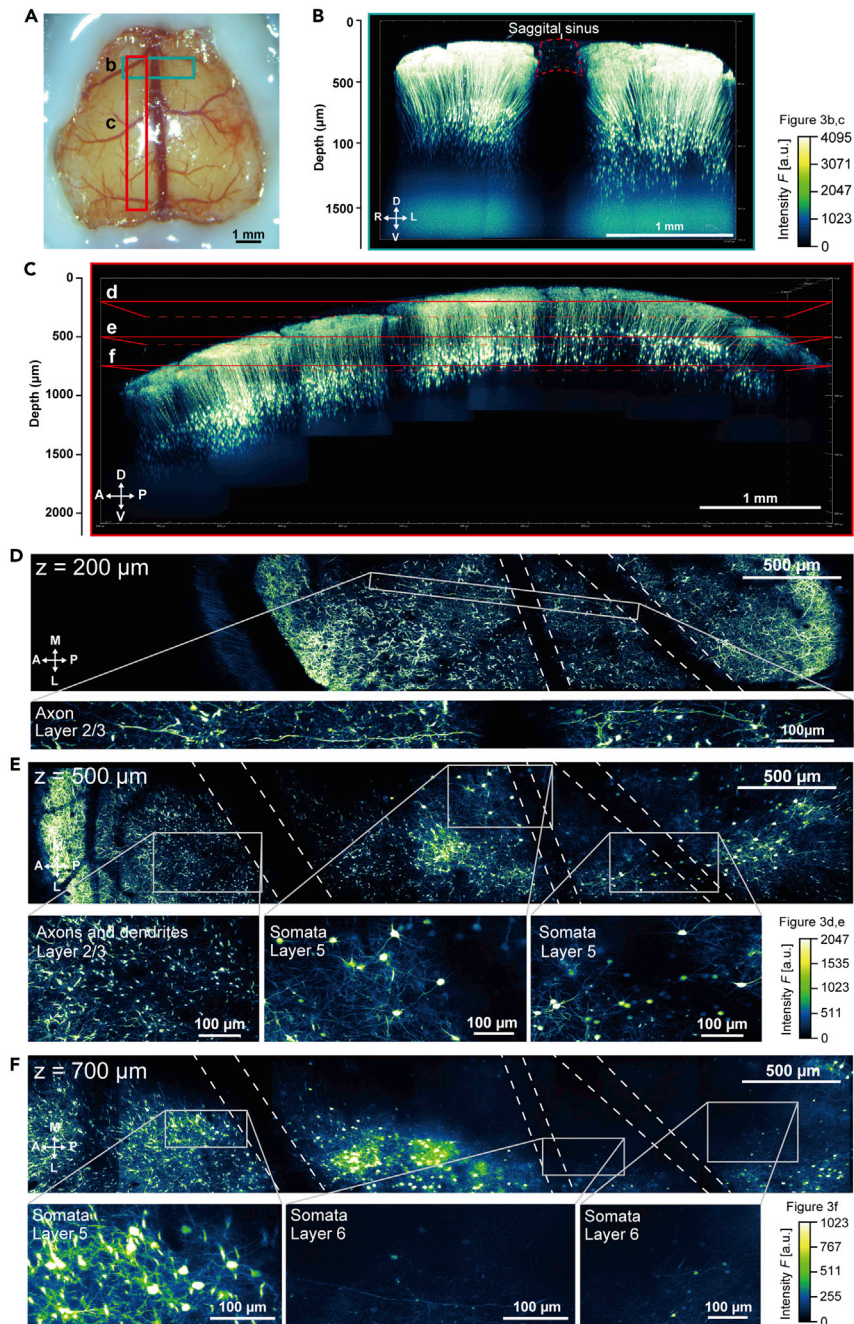
Figure 3. *In Vivo* Two-Photon Imaging in Thy1-EYFP-H #Mice with a Cranial Window Using the PEO-CYTOP Nanosheet

(A) Image of the brain of an H-line mouse with a cranial window with the PEO-CYTOP nanosheet. The regions within the green and red boxes are shown in detail in Figures 3B and 3C, respectively.

(B) Tomographic images tiled with the maximum intensity projections of the three-dimensional stacks as a coronal section shown as the green box in Figure 3A. The dotted lines roughly correspond to the region of the sagittal sinus and the invisible area under the sagittal sinus. Dorsal (D), ventral (V), right (R), and left (L) directions.

(C) Tomographic images tiled with the maximum intensity projections of the three-dimensional stacks as a sagittal section shown as the red box in Figure 3A. The red lines indicate the section of Figures 3D–3F. Dorsal (D), ventral (V), anterior (A), and posterior (P) directions.

(D) Cross-sectional xy-images of the axons or apical dendrites from a region located at a depth of 200 μm from the surface, as illustrated in Figure 3C. The dotted line indicates the invisible area under blood vessels.

Figure 3. *Continued*

(E) Cross-sectional *xy*-images of the pyramidal cell bodies or apical dendrites from a region located at a depth of 500 μm from the surface, as illustrated in Figure 3C. The dotted line indicates the invisible area under blood vessels.

(F) Cross-sectional *xy*-images of the pyramidal cell bodies from a region located at a depth of 700 μm from the surface, as illustrated in Figure 3C. The dotted line indicates the invisible area under blood vessels. Medial (M), lateral (L), anterior (A), and posterior (P) directions in (D, E, and F).

the fluorescent intensity changes, ΔF/F, resulting from Ca^{2+} elevations (Figures 5F and 5G). Neurons and astrocytes were classified according to the characteristics of the structure and the timescale of Ca^{2+} activity, as described previously (Stobart et al., 2018). The GCaMP7 signals of both neurons and astrocytes were observed even at 9 weeks after surgery.

To assess the suppression of inflammation by the PEO-CYTOP nanosheet, we immunostained activated astrocytes for the glial fibrillary acidic protein (GFAP) 2 weeks after surgery (Figure S8). To evaluate the degree of inflammation, the size of the areas that were occupied by activated astrocytes was assessed using Otsu's method (Otsu, 1979). We measured the percentage of the activated areas in regions of interest (ROIs) (unit area: 569 × 569 μm^2). Compared with glass coverslips, the PEO-CYTOP nanosheet suppressed the activated area of astrocytes significantly (0.014% ± 0.001%–0.006% ± 0.001%, mean ± standard error; n = 6 ROIs from two mice; p < 0.01 Student's t test) (Figure S8). Thus, the PEO-CYTOP nanosheet can be applied for long-term imaging while maintaining a healthy condition.

Long-Term Imaging Using the PEO-CYTOP Nanosheet with Removal of the Dura

Next, we evaluated whether the PEO-CYTOP nanosheet could be used as a substitute for the dura. Here, we attached a PEO-CYTOP nanosheet after the removal of the dura and placed a glass coverslip onto the nanosheet, to protect the cranial window for long-term imaging, as shown in Figure 5 (Figure 6A). In this case, the removal of the dura frequently triggered bleeding and injuries because of the dissection of blood vessels connecting the dura with the brain tissues. We confirmed that the PEO-CYTOP nanosheet could also suppress bleeding and injuries resulting from mechanical stress to the brain surface in the absence of the dura. In this window, we kept the optical transparency for 14 weeks post-surgery and did not observe dura regrowth or blood coagulation (Figure 6B). Moreover, we achieved long-term two-photon imaging in Thy1-EYFP-H mice in which the dura was replaced with a PEO-CYTOP nanosheet (Figures 6C and 6D). We were able to observe the same neuron and axon in the same period.

DISCUSSION

In this study, we successfully demonstrated that our newly developed PEO-CYTOP nanosheet enabled the visualization of the neural morphology and Ca^{2+} elevations with a broader FOV in the mouse brain (Figures 3 and 4); thus the PEO-CYTOP nanosheet is a material that is useful to seal cranial windows for the *in vivo* imaging of mouse brains.

The PEO-CYTOP nanosheet sealed the injured blood vessels tightly and suppressed bleeding from the brain surface because of the high adhesive strength of the nanosheet that resulted from physical adsorption, such as van der Waals interactions (Hagisawa et al., 2013; Komachi et al., 2017). Previously, several biocompatible nanosheets, including a poly(ʟ-lactic acid) nanosheet, were applied for the suppression of bleeding from various organs, including the stomach, liver, and inferior vena cava (Okamura et al., 2009; Hagisawa et al., 2013; Komachi et al., 2017). In contrast, CYTOP nanosheets exhibited potential as a material for living-tissue imaging because of their excellent water retention and surface adhesion. However, CYTOP nanosheets could not be attached firmly to the brain surface because of the high hydrophobicity of CYTOP (data not shown). To hydrophilize the surface of the nanosheet, we modified the adhesive surface of the CYTOP nanosheet by coating it with PDMS and attaching PEO (Figure 1). This hydrophilization of the nanosheet surface enhanced the strength of the adhesion to wet specimens, resulting in the suppression of bleeding from the brain surface (Figures S2 and 3). Thus, the PEO-CYTOP nanosheet may be helpful for the *in vivo* imaging of other living organs, other than the brain, by effectively preventing bleeding of the tissue.

The optical disturbance caused by the PEO-CYTOP nanosheet was almost negligible compared with the conventional glass coverslip, because the thickness of the PEO-CYTOP nanosheet was ∼10^{-3} smaller than that of the conventional glass coverslip (Holtmaat et al., 2009; Goldey et al., 2014) (PEO-CYTOP
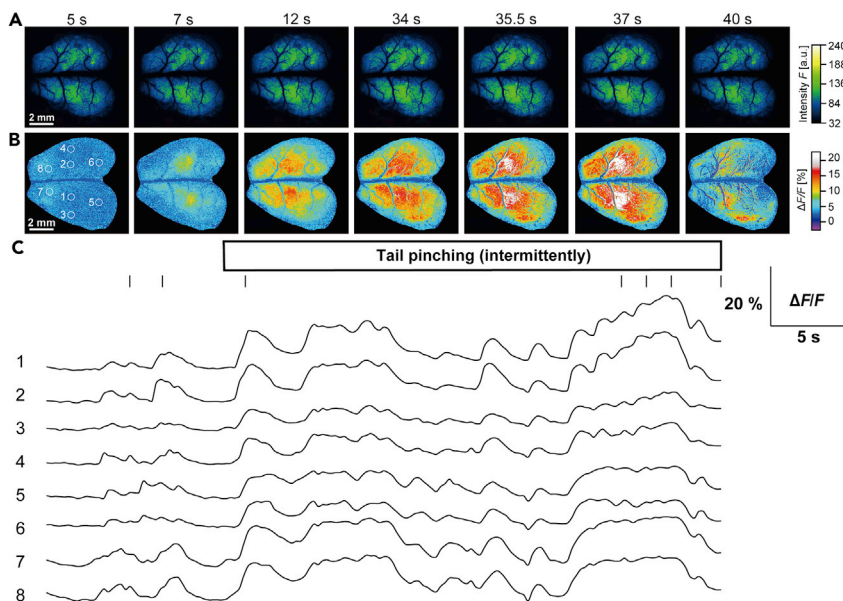
**Figure 4. Wide-field Imaging of GCaMP7 Using the PEO-CYTOP Nanosheet**

(A) Time-lapse fluorescence images of Ca^{2+} elevations in the mouse. The times are indicated using short solid lines in Figure 4C.

(B and C) (B) Time-lapse images of fluorescent intensity changes after tail pinching. The times are indicated using short solid lines in Figure 4C. The white squares and numbers represent the regions of interest (ROIs) for fluorescent intensity traces in Figure 4C. (C) Relative fluorescent intensity change ($\Delta F/F$) traces from the ROIs of Figure 4B. The short solid lines indicate the time of Figure 4B. In the second half of the trace, stimulation was applied by tail pinching.

nanosheet, ∼130 nm; conventional glass coverslip, ∼170 μm), and even smaller than the wavelength of visible light. In a method described previously based on a similar concept (Heo et al., 2016), a PDMS film with a thickness of 300 μm was applied. In contrast, the thickness of the PEO-CYTOP nanosheet used in this study was approximately 100 nm, which enables strong adhesiveness and suppression of inflammation and bleeding from the brain tissue by adhering closely. Moreover, the refractive index of CY-TOP is ∼1.34, which is mostly similar to that of water (∼1.33) but lower than that of glass (∼1.54) and PDMS (∼1.41). In addition, the PEO-CYTOP nanosheet had approximately 100% transmittance (Figure S1D). Therefore, the PEO-CYTOP nanosheet can be used as a sealing material for *in vivo* brain imaging with smaller effects from incident lights. Moreover, the water permeability of CYTOP was smaller than that of the PDMS per unit of thickness, which translated into the excellent water retention effect of the PEO-CY-TOP nanosheet, even at nano-order thickness.

In recent studies, the brain temperature affects blood flow and oxygen partial pressure in the brain (Roche et al., 2019). Therefore, we evaluated thermal property of PEO-CYTOP nanosheet. Considering the difference of the thickness between ∼130 nm (PEO-CYTOP) and ∼170 μm (glass coverslip) and the thermal conductivity between ∼0.12 W/mK (PEO-CYTOP) and ∼1.1 W/mK (glass coverslip), the cranial window of PEO-CYTOP is ∼80 times heat-transferable than glass coverslip. Thus, PEO-CYTOP nanosheet could control the brain temperature effectively. On the other hand, the brain temperature was affected by laser wavelength and power (Wang et al., 2020). However, there would be no problem related to the heat generation during two-photon imaging in this study.

To observe a living brain with a larger FOV, researchers have proposed novel microscopic instruments and techniques (Heo et al., 2016; Kim et al., 2016; Sofroniew et al., 2016; Terada et al., 2018). As shown in Figures 2 and 3, the flexibility and adhesiveness of the nanosheets also enlarged the window size, which was previously limited because the glass coverslips could not follow the curvature of the brain surface; thus, we were able to prepare a larger cranial window (diameter, over 8 mm) compared with the typical size (diameter, 2–5 mm) (Holtmaat et al., 2009; Goldey et al., 2014). Recently, novel regents for realizing the cranial window of optically transparent skull have been proposed (Zhao et al., 2018; Zhang et al., 2018a). The
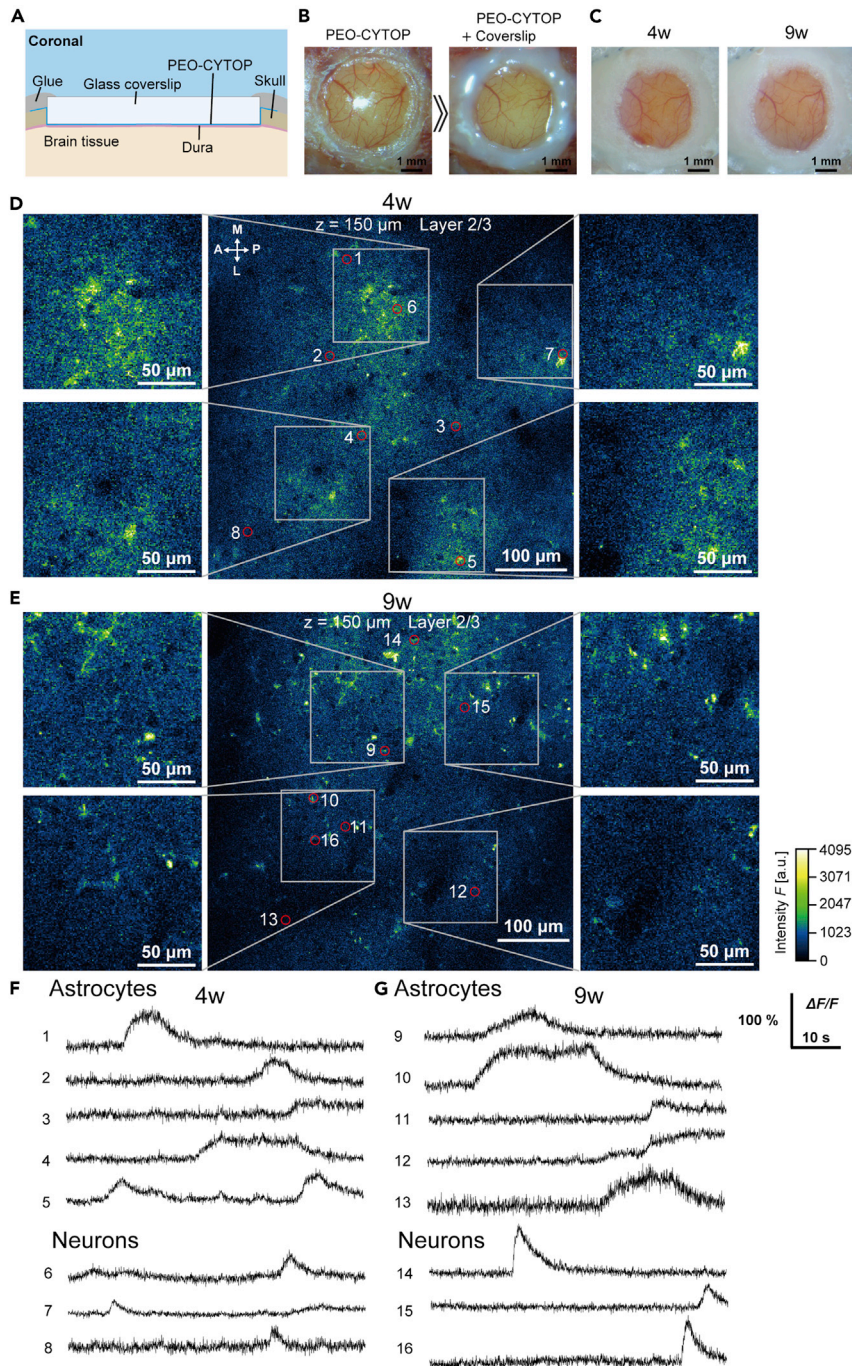
Figure 5. *In vivo* Ca²⁺ Imaging Using GCaMP7 with the PEO-CYTOP Nanosheet

(A) Schematic representation of the cranial window with the PEO-CYTOP nanosheet combined with a glass coverslip on the primary visual cortex (V1).

(B) Images of the cranial window with the PEO-CYTOP nanosheet combined with a glass coverslip on the V1 in a G7NG817 mouse.

(C) Images of the cranial window of Figure 5B up to 9 weeks post-surgery.

(D) Fluorescence images of Ca²⁺ elevations in the primary visual cortex layer 2/3 at 4 weeks post-surgery in the mouse, similar to Figure 5B. The red circles and white numbers represent the regions of interest (ROIs) used for the fluorescent intensity traces depicted in Figure 5F, respectively. Medial (M), lateral (L), anterior (A), and posterior (P) directions.

Figure 5. *Continued*

(E) Fluorescence images of Ca^{2+} elevations in the primary visual cortex layer 2/3 at 9 weeks post-surgery in the mouse, similar to Figure 5C. The red circles and white numbers represent the ROIs used for the fluorescent intensity traces depicted in Figure 5G, respectively. Medial (M), lateral (L), anterior (A), and posterior (P) directions.

(F and G) (F) Relative fluorescence change (*ΔF/F*) traces of Ca^{2+} transients from the ROIs depicted in Figure 5D, respectively. The numbers represent the ROIs shown in Figure 5D. (G) Relative fluorescence change (*ΔF/F*) traces of Ca^{2+} transients from the ROIs depicted in Figure 5E, respectively. The numbers represent the ROIs shown in Figure 5E.

procedure was less invasive and did not require complicated surgical processes. Some modulations may be required for observing the deeper regions, which was achieved by traditional cranial windows.

As shown in Figure S6, the glass coverslips suppressed the motion artifacts by pressing the brain surface tightly. However, the glass coverslips were not suitable for preserving the physiological conditions because the brain tissue was forcefully flattened. Conversely, the PEO-CYTOP nanosheet probably preserved the physiological conditions, thus potentially providing an absence of mechanical stress inside the brain and no disturbance of the flow of cerebrospinal fluid and blood.

In contrast, a cranial window with a large FOV is potentially prone to optical aberrations, such as coma or astigmatism, resulting from the curvature of the living brain surface. A planar glass coverslip is suitable for reducing these aberrations; however, a large cranial window cannot be sealed with a planar glass coverslip, because the physiological condition is deteriorated. Combined with novel adaptive optical techniques (Tanabe et al., 2016; Matsumoto et al., 2018), the PEO-CYTOP nanosheet might realize wide-field imaging at higher resolution.

The results presented in Figures 5 and S8 demonstrated that the PEO-CYTOP nanosheet can be applied for long-term imaging of the living mouse brain without causing severe inflammation or bleeding. The PEO-CYTOP nanosheet protected the brain surface from contacting with foreign substances that caused inflammation, such as fine dust, mouse hairs, and glue to fix the sealing materials in the operation. Moreover, the chemical property of CYTOP avoids the decomposition of the nanosheet during long-term imaging because CYTOP is a chemically inert and non-biodegradable fluoropolymer (Leis et al., 2005). In addition, PEO is highly biocompatible to be used as a coating material for medical equipment in general, because hydrated water molecules on the PEO surface might suppress inflammatory reactions (Ikeda and Nagasaki, 2014). Therefore, the PEO surface of the nanosheet probably inhibited the inflammation compared with a glass surface. This result was also supported by previous studies that indicated that biocompatible nanosheets inhibited inflammation and bleeding in living tissues (Okamura et al., 2013; Hagisawa et al., 2013). Moreover, no unusual behaviors or symptoms of infection were observed in the mice over 1 year post-surgery (data not shown). Thus, the PEO-CYTOP nanosheet may be helpful to realize wide-field long-term imaging in combination with novel techniques for the creation of large cranial windows (Heo et al., 2016; Kim et al., 2016).

Even in the case of the PEO-CYTOP nanosheet, proliferation of connective tissues and immune cells or regrowth of the dura sometimes occurred 2–4 weeks after surgery (data not shown) (Shih et al., 2012; Goldey et al., 2014; Coles et al., 2017). In this study, by replacing the dura with the PEO-CYTOP nanosheet, these effects were remarkably suppressed. Previously, researchers have reported several artificial dura substitutes composed of biocompatible polymers, including PDMS, that can inhibit inflammation and maintain healthy conditions in the mammalian brain after removal of the dura (Arieli et al., 2002; Jackson and Muthuswamy, 2008; Heo et al., 2016). Especially in rats and marmosets, the removal of the dura is required for *in vivo* two-photon imaging because it is much thicker and opaque than that of mice (Stettler et al., 2006; Gimsa et al., 2011). Thus, the PEO-CYTOP nanosheet may be useful for *in vivo* two-photon imaging as an artificial dura substitute in various animals.

In a previous study, a porous nanosheet allowed drugs to permeate into the sealed object (Zhang et al., 2018b). It would also be possible to administer drugs to nanosheet-sealed objects using solid inserts, including a microcapillary or a needle. Moreover, the PEO-CYTOP nanosheet would be applicable to the simultaneous recording of *in vivo* fluorescence images and electrophysiological data, because of its tolerance regarding the insertion of solid electrodes.

In summary, our newly developed PEO-CYTOP nanosheet realized *in vivo* deep and wide-field imaging of the living mouse brain. This novel technique may promote the understanding of the functional connectivity
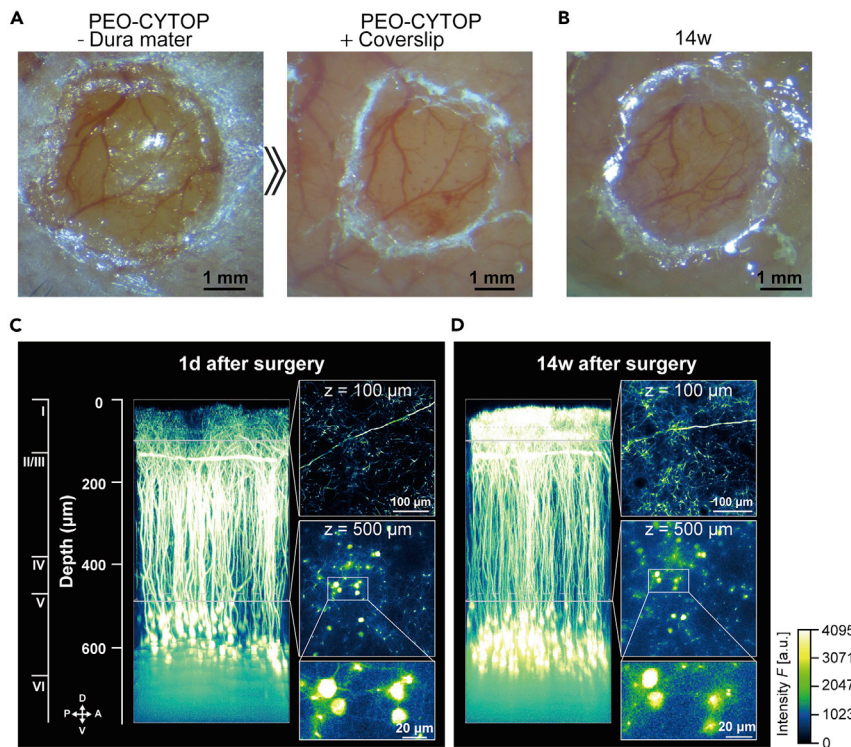
Figure 6. *In Vivo* Two-Photon Imaging Using the PEO-CYTOP Nanosheet with Removal of the Dura
(A) Images of the cranial window with the PEO-CYTOP nanosheet and the combination of the nanosheet with a glass coverslip on the visual cortex (V1) in the H-line mouse
(B) Images of the cranial window shown in Figure 6A up to 14 weeks post-surgery.
(C) Maximum intensity projections of the two-photon fluorescence images in the same mouse as that shown in Figure 6A at 1 day post-surgery.
(D) Maximum intensity projections of the two-photon fluorescence images in the same mouse as that used in Figure 6A at 14 weeks post-surgery. Dorsal (D), ventral (V), anterior (A), and posterior (P) directions in (C and D).

between multiple cortical regions in living animal brains by improving the surgical procedure and expanding the optically observable regions.

Limitations of the Study

There are two major points to be improved for *in vivo* imaging utilizing a PEO-CYTOP nanosheet. First, the PEO-CYTOP nanosheet cannot suppress the displacement of the FOV as shown in Figure S6. To improve the stability of the FOV against motion artifacts, optical systems proposed previously for real-time movement correction could be adopted (Karagyozov et al., 2018; Griffiths et al., 2020). Second, a large cranial window using PEO-CYTOP nanosheet did not affect the natural curvature of the living brain surface but caused optical aberrations. To compensate them, adaptive optical techniques proposed previously should be adopted (Tanabe et al., 2016; Matsumoto et al., 2018; Yamaguchi et al., 2020).

Resource Availability

Lead Contact

Further information and requests for resources and reagents should be directed to and will be fulfilled by the Lead Contact, Tomomi Nemoto (tn@nips.ac.jp).

Materials Availability

PEO-CYTOP nanosheet will be made available on reasonable requests, but we may require a payment and/or a completed Materials Transfer Agreement.

Data and Code Availability

The data and code supporting the current study have not been deposited in a public repository but are available from the corresponding author on reasonable requests.

SUPPLEMENTAL INFORMATION

Supplemental Information can be found online at https://doi.org/10.1016/j.isci.2020.101579.

AUTHOR CONTRIBUTIONS

T.T., R.K., Y.O., H.Z., K.Y., K.O., and T.N. designed the method and the imaging experiments. T.T. performed the imaging experiments and the analysis. M.A. and J.N. made the analysis program for evaluation of motion artifact. Y.O., H.Z., and K.Y. developed and fabricated the surface-modified fluoropolymer nanosheets. T.T., H.Z., Y.O., R.K., K.O., and T.N. designed and wrote the manuscript.

DECLARATION OF INTERESTS

The authors declare no competing interests.

REFERENCES

Arieli, A., Grinvald, A., and Slovin, H. (2002). Dural substitute for long-term imaging of cortical activity in behaving monkeys and its clinical implications. J. Neurosci. Methods 114, 119–133.

Coles, J.A., Stewart-Hutchinson, P.J., Myburgh, E., and Brewer, J.M. (2017). The mouse cortical meninges are the site of immune responses to many different pathogens, and are accessible to intravital imaging. Methods 127, 53–61.

Denk, W., Strickler, J.H., and Webb, W.W. (1990). Two-photon laser scanning fluorescence microscopy. Science 248, 73–76.

Ebina, T., Masamizu, Y., Tanaka, Y.R., Watakabe, A., Hirakawa, R., Hirayama, Y., Hira, R., Terada,

S.-I., Koketsu, D., Hikosaka, K., et al. (2018). Two-photon imaging of neuronal activity in motor cortex of marmosets during upper-limb movement tasks. Nat. Commun. 9, 1879.

Feng, G., Mellor, R.H., Bernstein, M., Keller-Peck, C., Nguyen, Q.T., Wallace, M., Nerbonne, J.M., Lichtman, J.W., and Sanes, J.R. (2000). Imaging neuronal subsets in transgenic mice expressing multiple spectral variants of GFP. Neuron 28, 41–51.

Fujie, T., Kinoshita, M., Shono, S., Saito, A., Okamura, Y., Saitoh, D., and Takeoka, S. (2010). Sealing effect of a polysaccharide nanosheet for murine cecal puncture. Surgery 148, 48–58.

Ghanbari, L., Carter, R.E., Rynes, M.L., Dominguez, J., Chen, G., Naik, A., Hu, J., Sagar, M.A.K., Haltom, L., Mossazghi, N., et al. (2019). Cortex-wide neural interfacing via transparent polymer skulls. Nat. Commun. 10, 1500.

Gimsa, U., Nowak, K., Mix, E., Gimsa, J., Strauss, U., Sriperumbudur, K.K., and Benecke, R. (2011). Optimizing a rodent model of Parkinson's disease for exploring the effects and mechanisms of deep brain stimulation. Parkinsons. Dis. 2011, 414682.

Goldey, G.J., Roumis, D.K., Glickfeld, L.L., Kerlin, A.M., Reid, R.C., Bonin, V., Schafer, D.P., and Andermann, M.L. (2014). Removable cranial

windows for long-term imaging in awake mice. Nat. Protoc. *9*, 2515–2538.

Griffiths, V.A., Valera, A.M., Lau, J.Y., Roš, H., Younts, T.J., Marin, B., Baragli, C., Coyle, D., Evans, G.J., Konstantinou, G., et al. (2020). Real-time 3D movement correction for two-photon imaging in behaving animals. Nat. Methods *17*, 741–748.

Hagisawa, K., Saito, A., Kinoshita, M., Fujie, T., Otani, N., Shono, S., Park, Y.-K., and Takeoka, S. (2013). Effective control of massive venous bleeding by 'multioverlapping therapy' using polysaccharide nanosheets in a rabbit inferior vena cava injury model. J. Vasc. Surg. Venous Lymphat. Disord. *1*, 289–297.

Helmchen, F., and Denk, W. (2005). Deep tissue two-photon microscopy. Nat. Methods *2*, 932–940.

Heo, C., Park, H., Kim, Y.T., Baeg, E., Kim, Y.H., Kim, S.G., and Suh, M. (2016). A soft, transparent, freely accessible cranial window for chronic imaging and electrophysiology. Sci. Rep. *6*, 27818.

Holtmaat, A., Bonhoeffer, T., Chow, D.K., Chuckowree, J., De Paola, V., Hofer, S.B., Hübener, M., Keck, T., Knott, G., Lee, W.-C., et al. (2009). Long-term, high-resolution imaging in the mouse neocortex through a chronic cranial window. Nat. Protoc. *4*, 1128–1144.

Ikeda, Y., and Nagasaki, Y. (2014). Impacts of PEGylation on the gene and oligonucleotide delivery system. J. Appl. Polym. Sci. *131*, 40293.

Jackson, N., and Muthuswamy, J. (2008). Artificial dural sealant that allows multiple penetrations of implantable brain probes. J. Neurosci. Methods *171*, 147–152.

Karagyozov, D., Mihovilovic Skanata, M., Lesar, A., and Gershow, M. (2018). Recording neural activity in unrestrained animals with three-dimensional tracking two-photon microscopy. Cell Rep. *25*, 1371–1383.

Kim, T.H., Zhang, Y., Lecoq, J., Jung, J.C., Li, J., Zeng, H., Niell, C.M., and Schnitzer, M.J. (2016). Long-term optical access to an estimated one million neurons in the live mouse cortex. Cell Rep. *17*, 3385–3394.

Komachi, T., Sumiyoshi, H., Inagaki, Y., Takeoka, S., Nagase, Y., and Okamura, Y. (2017). Adhesive and robust multilayered poly(lactic acid) nanosheets for hemostatic dressing in liver injury model. J. Biomed. Mater. Res. B Appl. Biomater. *105*, 1747–1757.

Kondo, M., Kobayashi, K., Ohkura, M., Nakai, J., and Matsuzaki, M. (2017). Two-photon calcium imaging of the medial prefrontal cortex and hippocampus without cortical invasion. Elife *6*, e26839.

Leis, A.P., Schlicher, S., Franke, H., and Strathmann, M. (2005). Optically transparent porous medium for nondestructive studies of microbial biofilm architecture and transport dynamics. Appl. Environ. Microbiol. *71*, 4801–4808.

Matsumoto, N., Konno, A., Inoue, T., and Okazaki, S. (2018). Aberration correction considering curved sample surface shape for non-contact two-photon excitation microscopy with spatial light modulator. Sci. Rep. *8*, 9252.

Monai, H., Ohkura, M., Tanaka, M., Oe, Y., Konno, A., Hirai, H., Mikoshiba, K., Itohara, S., Nakai, J., Iwai, Y., et al. (2016). Calcium imaging reveals glial involvement in transcranial direct current stimulation-induced plasticity in mouse brain. Nat. Commun. *7*, 11100.

Nemoto, T., Kawakami, R., Hibi, T., Iijima, K., and Otomo, K. (2015). Two-photon excitation fluorescence microscopy and its application in functional connectomics. Microscopy *64*, 9–15.

Okamura, Y., Kabata, K., Kinoshita, M., Saitoh, D., and Takeoka, S. (2009). Free-standing biodegradable poly(lactic acid) nanosheet for sealing operations in surgery. Adv. Mater. *21*, 4388–4392.

Okamura, Y., Kabata, K., Kinoshita, M., Miyazaki, H., Saito, A., Fujie, T., Ohtsubo, S., Saitoh, D., and Takeoka, S. (2013). Fragmentation of poly (lactic acid) nanosheets and patchwork treatment for burn wounds. Adv. Mater. *25*, 545–551.

Okano, H., Sasaki, E., Yamamori, T., Iriki, A., Shimogori, T., Yamaguchi, Y., Kasai, K., and Miyawaki, A. (2016). Brain/MINDS: A Japanese national brain project for marmoset neuroscience. Neuron *92*, 582–590.

Otsu, N. (1979). A threshold selection method from gray level histograms. IEEE Trans. Syst. Man Cybern. *9*, 62–66.

Roche, M., Chaigneau, E., Rungta, R.L., Boido, D., Weber, B., and Charpak, S. (2019). In vivo imaging with a water immersion objective affects brain temperature, blood flow and oxygenation. Elife *8*, e47324.

Shih, A.Y., Driscoll, J.D., Drew, P.J., Nishimura, N., Schaffer, C.B., and Kleinfeld, D. (2012). Two-photon microscopy as a tool to study blood flow and neurovascular coupling in the rodent brain. J. Cereb. Blood Flow Metab. *32*, 1277–1309.

Sofroniew, N.J., Flickinger, D., King, J., and Svoboda, K. (2016). A large field of view two-photon mesoscope with subcellular resolution for in vivo imaging. Elife *5*, e14472.

Someya, D., Arai, S., Fujie, T., and Takeoka, S. (2018). Extracellular pH imaging of a plant leaf with a polyelectrolyte multilayered nanosheet. RSC Adv. *8*, 35651–35657.

Sporns, O., Tononi, G., and Kötter, R. (2005). The human connectome: a structural description of the human brain. PLoS Comput. Biol. *1*, e42.

Stettler, D.D., Yamahachi, H., Li, W., Denk, W., and Gilbert, C.D. (2006). Axons and synaptic boutons are highly dynamic in adult visual cortex. Neuron *49*, 877–887.

Stobart, J.L., Ferrari, K.D., Barrett, M.J.P., Glück, C., Stobart, M.J., Zuend, M., and Weber, B. (2018). Cortical circuit activity evokes rapid astrocyte calcium signals on a similar timescale to neurons. Neuron *98*, 726–735.

Tanabe, A., Hibi, T., Ipponjima, S., Matsumoto, K., Yokoyama, M., Kurihara, M., Hashimoto, N., and Nemoto, T. (2016). Transmissive liquid-crystal device for correcting primary coma aberration and astigmatism in biospecimen in two-photon excitation laser scanning microscopy. J. Biomed. Opt. *21*, 121503.

Terada, S.I., Kobayashi, K., Ohkura, M., Nakai, J., and Matsuzaki, M. (2018). Super-wide-field two-photon imaging with a micro-optical device moving in post-objective space. Nat. Commun. *9*, 3550.

Theer, P., Hasan, M.T., and Denk, W. (2003). Two-photon imaging to a depth of 1000 μm in living brains by use of a Ti:Al$_2$O$_3$ regenerative amplifier. Opt. Lett. *28*, 1022.

Wang, T., Wu, C., Ouzounov, D.G., Gu, W., Xia, F., Kim, M., Yang, X., Warden, M.R., and Xu, C. (2020). Quantitative analysis of 1300-nm three-photon calcium imaging in the mouse brain. Elife *9*, e53205.

Yamaguchi, K., Kitamura, R., Kawakami, R., Otomo, K., and Nemoto, T. (2020). In vivo two-photon microscopic observation and ablation in deeper brain regions realized by modifications of excitation beam diameter and immersion liquid. PLoS One *15*, e0237230.

Zhang, H., Masuda, A., Kawakami, R., Yarinome, K., Saito, R., Nagase, Y., Nemoto, T., and Okamura, Y. (2017). Fluoropolymer nanosheet as a wrapping mount for high-quality tissue imaging. Adv. Mater. *29*, 1703139.

Zhang, C., Feng, W., Zhao, Y., Yu, T., Li, P., Xu, T., Luo, Q., and Zhu, D.A. (2018a). A large, switchable optical clearing skull window for cerebrovascular imaging. Theranostics *8*, 2696–2708.

Zhang, H., Aoki, T., Hatano, K., Kabayama, K., Nakagawa, M., Fukase, K., and Okamura, Y. (2018b). Porous nanosheet wrapping for live imaging of suspension cells. J. Mater. Chem. B *6*, 6622–6628.

Zhao, Y., Yu, T., Zhang, C., Li, Z., Luo, Q., Xu, T., and Zhu, D. (2018). Skull optical clearing window for in vivo imaging of the mouse cortex at synaptic resolution. Light Sci. Appl. *7*, 17153.

Supplemental Information

PEO-CYTOP Fluoropolymer Nanosheets

as a Novel Open-Skull Window

for Imaging of the Living Mouse Brain

Taiga Takahashi, Hong Zhang, Ryosuke Kawakami, Kenji Yarinome, Masakazu Agetsuma, Junichi Nabekura, Kohei Otomo, Yosuke Okamura, and Tomomi Nemoto

Transparent Methods

Fabrication of surface-modified fluoropolymer nanosheets

The perfluoro (1-butenyl vinyl ether) polymer, which is commercially known as CYTOP (CTX-809SP, AGC Inc., Japan), was dissolved in perfluorotributylamine at a concentration of 30 mg/mL, for spin casting. The substrates were silicon wafers (100) deposited on a 200 nm silicon oxide layer (KST World Corp., Japan) that were freshly cut into an appropriate size before use. PVA (M_w, 22,000; Kanto Chemical Co., Inc., Japan) in water at 10 mg/mL was dropped onto a substrate and spin coated at 4000 rpm for 20 s (MS-A100, Mikasa Co., Ltd., Japan), to prepare a sacrificial layer. Subsequently, the CYTOP solution was dropped onto a PVA-coated substrate and spin coated at 4000 rpm for 60 s. A 10:1 w/w mixture of Sylgard 184 silicone elastomer base and curing agent was dissolved in hexane at a concentration of 1.25 wt% and spin coated at 4000 rpm for 20 s. The composite was cured at 80 °C for 2 h and then exposed to oxygen plasma at 11 W for 60 s (PDC-32G, Harrick Plasma, Inc., NY, USA). PEO-silane (2-(methoxy(polyethyleneoxy)propyl) trichlorosilane; SIM6492.66; M_w, ~538; Gelest, Inc., PA, USA) was dissolved in toluene at 2 mM for the modification of the hydrophilic surface. The resulting substrate was placed in a Teflon dish filled with silane solution at room temperature (25 °C) for 1 h. Finally, the prepared nanosheets were released from the substrate to float on the surface of the water as the sacrificial layer dissolved and were re-supported on a required surface for subsequent characterization. It is worth noting that, to adhere the nanosheet to a living mouse brain, they were transferred to the surface of a nonwoven fabric

substrate (disposable tea filter bag made from polyethylene and polypropylene, complied with Japanese Food Sanitation Act, Product Code: H-070 No. 475, Daiso Industries Co., Ltd.), with the hydrophilic side facing outward.

Characterization of the fluoropolymer nanosheets

The thickness of the nanosheets on the silicon wafer was analyzed using a stylus profilometer (DektakXT, Bruker Corp., MA, USA) and estimated as ~130 nm (Figure S1e). The morphology of the nanosheets on the Anodisc membrane (pore size, 0.1 µm; GE Healthcare, IL, USA) was observed via field-emission SEM (S-4800; Hitachi High-Technologies Corp., Japan). The static water contact angle of the nanosheets was measured using a contact angle meter (DMe-211, Kyowa Interface Science Co., Ltd., Japan) at room temperature and relative humidity of 40%. A surface element analysis of the nanosheets was performed before and after surface modification using X-ray photoelectron spectroscopy (PHI Quantera II, Physical Electronics, Inc., MN, USA). The light transmittance of the nanosheets supported on the quartz glass was measured using a UV-Vis-NIR spectrophotometer (V-670, JASCO Corp., Japan) at a wavelength of 300–800 nm. The water-retention effect of the nanosheet was evaluated as reported previously (Zhang *et al.*, 2017). Specifically, a sodium alginate (Kanto Chemical Co., Inc.) aqueous solution at 20 mg/mL was poured into a calcium chloride solution at 2 wt% with a ratio of 1:2 v/v. An alginate hydrogel ball was formed after stirring overnight. Subsequently, the hydrogel was punched into a cylindrical shape with a diameter of 10 mm and a thickness of 3 mm, which was gently placed in the center of a floating nanosheet on the surface of the water with the

addition of 100 µL of water. A cover slip with a diameter of 25 mm and a thickness of 0.13–0.16 mm (AS ONE Corp., Japan) was pressed from above and then enfolded in the margin of the nanosheet using tweezers. The original weight of the wrapped samples at specific time intervals over 24 h at room temperature and at a relative humidity of 40% was measured as W_0 and W_t, respectively. The sample was then thoroughly dried in an oven at 80 °C and weighed as W_d. The water retention ratio was obtained using the following equation: $(W_t - W_d) / (W_0 - W_d) \times 100$ wt%. Moreover, we developed a method to evaluate the improved adhesion capability of the nanosheets after surface modification. Herein, the suspension of MNPs with a diameter of 10 nm (EMG 707; Ferrotec Corp., CA, USA) was mixed with the sodium alginate solution at a 1:1 v/v ratio, and the MNP-loaded hydrogel with a diameter of 3 mm was prepared as a model of the tissue. To prevent the desiccation of the hydrogel and to stimulate the tissue fluid that leaked out of the mouse brain, 1 µL water was dropped before the hydrogel was placed on the surface of the nanosheet. A permanent magnet (remanence magnetic flux density, ~480 mT) was gradually placed closer to the sample, until the hydrogel could overcome the maximum friction. The distance over which the hydrogel was dragged was termed the resistant distance, d, which was determined based on a movie captured by a digital camera (G7 X Mark II; Canon Inc., Japan).

Animals

We used adult (over 8 weeks of age) mice for all experiments. All mice were housed under a 12 h/12 h light/dark cycle. We used wild-type and Thy1-EYFP-H

(H-line) transgenic mice for *in vivo* imaging in this study (Feng *et al.*, 2000). H-line mice, which express the enhanced yellow fluorescent protein (EYFP) in a subset of layer 5 pyramidal cells, enabled us to achieve fluorescence images that were suitable for evaluating the differences in the structure of neurons, as well as an optically accessible depth for two-photon microscopy. G7NG817 transgenic mice expressing the Ca^{2+} indicator GCaMP7 in astrocytes and a subpopulation of neurons were used to evaluate brain function (Monai *et al.*, 2016). This study was carried out in accordance with the recommendations included in the Guidelines for the Care and Use of Laboratory Animals of the Animal Research Committee of Hokkaido University. The procedures were approved by the Institutional Animal Care and Use Committee of the National University Corporation Hokkaido University (Permit Number: 17-0077). These genetic recombination experiments were approved by the Safety Committee on Genetic Recombination Experiments of Hokkaido University (Permit Number: 2017-037). The facility used for the care and management of laboratory animals was approved by the Institutional Animal Care and Use Committee of Hokkaido University (Permit Number: 29(6)).

Cranial window surgery

The mouse was anesthetized with 1%–2% isoflurane during surgery. The body temperature of the mouse was maintained using a heating light or a heating mat. First, the hair and skin of the mouse were removed to expose the cranial skull. Subsequently, part of the cranial skull was removed to generate a cranial window for high-resolution imaging in the living mouse brain. For the removal of

the dura, we administered 20% mannitol (10 μL/g, TERUMO Corp., Japan) via intraperitoneal injection, to loosen the dura for 30 min before the surgery. We then made a rift in the dura using a tweezer or a 27G needle and carefully inserted a tweezer under the dura via the rift, to peel it off. To stain astrocytes using sulforhodamine 101 (SR101), we directly dropped 25 μM SR101 onto the brain surface and incubated it for 5 min. After washing dust and blood off the skull using phosphate-buffered saline (PBS) or saline, we placed the PEO-CYTOP nanosheet supported by a nonwoven fabric onto the brain surface and attached the hydrophilic side to the brain surface. The PEO-CYTOP nanosheet was then lightly pushed via the nonwoven fabric using a tweezer, for adherence to the brain surface. After confirming that the PEO-CYTOP nanosheet had been transferred to the brain surface, the nonwoven fabric was removed. If misplacement of the nanosheet occurred, we were able to easily remove it by dropping PBS or saline onto it and floating the nanosheet from the brain surface. If a bubble was observed under the PEO-CYTOP nanosheet, we carefully pushed the bubble out using a tweezer or string made from a twisted Kimwipe (NIPPON PAPER CRECIA Co., Ltd., Japan). In large cranial windows in particular, we administered 20% mannitol (10 μL/g) via intraperitoneal injection, to render the surface as flat as possible by reducing the intracranial pressure. After attaching it, the nanosheet was adjusted to the specified range of the cranial window. The edge of the sheet was glued using cyanoacrylate or UV-curable resin, to prevent soaking of the immersion solution under the PEO-CYTOP nanosheet (Figure 3a). When fixing the PEO-CYTOP nanosheet, the

resins remained localized at the edge of the nanosheet because CYTOP exhibits chemical resistance and repellency to both water and oil. However, in the case of observations performed using an air-immersion objective lens, the PEO-CYTOP nanosheet and its edge did not require sealing with the resins. For long-term imaging, we combined a PEO-CYTOP nanosheet with a glass cover slip, to prevent the PEO-CYTOP nanosheet from floating and breaking. Finally, a 35 mm disposable dish was fixed onto the head of the mouse, to preserve the immersion solution and suspend the head from the adapter stage, as reported previously (Kawakami *et al.*, 2013, 2015). Moreover, for long-term imaging, we set a glass cover slip (a circle with a diameter of 4.2 mm, as shown in Figures 5 and S6, S7; a circle with a diameter of 2.7 mm, as shown in Figure 6; and a 5 × 6 mm rectangle, as shown in Figure S5; #1S, approximately 0.17 mm in thickness, Matsunami Glass Ind., Ltd, Japan) on top of the PEO-CYTOP nanosheet, followed by similar procedures. To examine a brain tissue without any sealing materials, we made an annular bank surrounding the cranial hole and filled it with saline (Figure S7). We placed a glass cover slip on the top of the bank to avoid direct contact with the brain surface for preventing drying during 3 days after the surgery.

Removal and resealing of surface-modified fluoropolymer nanosheets

As shown in Figure S2, we introduced a crack in the PEO-CYTOP nanosheet, to allow the flowing of water into the gap between the adhesive surface of the nanosheet and the brain surface). By adding a large amount of water, the PEO-

CYTOP nanosheet was slightly separated from the brain surface by floating; thus, the floating nanosheet could be easily removed with tweezers. After removing the PEO-CYTOP nanosheet, another PEO-CYTOP nanosheet could be attached to the surface of the brain.

As shown in Figure S5, we prepared a similar cranial window that was sealed using either a glass cover slip or a PEO-CYTOP nanosheet, in turn. In this process, we (i) generated a cranial window using a PEO-CYTOP nanosheet and performed two-photon imaging, (ii) removed the PEO-CYTOP nanosheet, and (iii) resealed the cranial hole using a glass cover slip and performed two-photon imaging.

In vivo imaging

All two-photon fluorescence images were obtained by two-photon laser microscopy customized for *in vivo* imaging (A1R-MP+, Nikon). We used a Nikon CFI75 LWD 16×/0.80 NA (~800 × ~800 µm scanning area) water-immersion objective lens for broad cross-sectional imaging (e.g., Figure 3b–f) or a Nikon Apo LWD 25×/1.10 NA (~500 × ~500 µm scanning area) water-immersion objective lens for deep *in vivo* imaging (e.g., Figures 5, 6, and S5). When using glass cover slips, the correction collar of the objective lens was adjusted by rotating to 0.17. The refractive index of the immersion solution was changed using glycerin, which has a refractive index of ~1.47. A Ti:Sapphire laser (MaiTai eHP DeepSee, Spectra Physics) was employed as an excitation laser light source at a wavelength of 960 nm for EYFP and 920 nm for GCaMP7. Image stacks were acquired with Z-steps of 1 or 5 µm and 512 × 512 pixels. All

fluorescence signals under the 690 nm wavelength were detected by non-descanned detectors equipped with GaAsP PMTs (NDD) at 1 frame per second (fps) for EYFP or 30 fps for GCaMP7. We adjusted the sensitivity of the NDD and the laser power according to the experiments.

To measure wide-field Ca^{2+} elevations (e.g., Figure 4), we used epifluorescence microscopy (AZ100, Nikon) with a Nikon AZ-Plan Fluor 2×/0.20 NA air-immersion objective lens and a mercury lamp (Intensilight C-HGFI, Nikon) as the excitation laser light source. The fluorescence signals were detected using a CMOS camera (Zyla-5.5, Andor) with an FOV of 16.4 mm × 14.0 mm (2560 × 2160 pixels) at 3.8 fps.

With the exception of Figure S6, the results of two-photon imaging (e.g., Figures 3–6 and S5) were obtained from a mouse under anesthesia. In Figure S6, we utilized a custom-made head-fixation system for anesthetized or awake mice. The body temperature of the mouse was maintained by a disposable heating pad during imaging.

Fluorescent bead imaging

Yellow–green beads (diameter, 200 nm; Invitrogen) were embedded in 1% agarose gel (1:100, v/v). Image stacks were acquired with Z-steps of 0.2 µm and 512 × 512 pixels. The fluorescent bead images had a pixel size of 50 nm. FWHM values were calculated by fitting the fluorescence intensity profiles around the central intensity using Gaussian functions in ImageJ. We used a Nikon Apo LWD 25×/1.10 NA water-immersion objective lens for two-photon laser microscopy (A1R-MP+, Nikon).

Immunostaining

Mouse brains were perfusion-fixed with 4.0% paraformaldehyde (PFA). After overnight post-fixation in 4% PFA, coronal slices (50 µm) were prepared using a vibratome (7000smz; Campden Instruments Ltd, Leicestershire, UK). The fixed brain slices were then incubated in 10% blocking solution (NACALAI TESQUE, INC., Japan) containing 0.2% Triton X-100 for 30 min at room temperature, followed by incubation with primary antibodies (1:1,000 for anti-GFAP and 1:500 for anti-IBA-1 antibodies) overnight (~16 h) at 4 °C. After washing with 0.1% Tween 20 in PBS, the slices were incubated with secondary antibodies (1:500; Alexa Fluor 594 donkey anti-mouse IgG and Alexa Fluor 633 donkey anti-rabbit IgG; Thermo Fisher Scientific, Waltham, MA, USA) for 4 h at room temperature. Immunostained slices were examined using confocal microscopy (Leica TCS SP8 STED 3X FALCON, Leica, USA) with an HC PL Fluotar 20×/0.50 NA air-immersion objective lens.

The areas of activated astrocytes were measured using a NIS element (Ver.4.51, Nikon instrument INC., Japan). The size of the areas that were occupied by activated astrocytes was evaluated using Otsu's method (Otsu, 1979). The rate was calculated as activated areas in regions of interest (ROIs) per ~569 × ~569 μm^2 (500 × 500 px).

Data analysis

The correlation coefficient used in Figure S6 was calculated by MATLAB (The MathWorks, Inc., USA). The reference frames defined by (i) generating a reference frame as the median of all frames, (ii) calculating the correlation

coefficient from the reference frame of (i), (iii) generating a reference frame again using the median of 10 frames from the top correlation coefficient of (ii), and (iv) calculating the correlation coefficient from the reference frame of (iii).

GCaMP7 images were analyzed using an imaging software (NIS element Ver.4.51, Nikon). The Time Measurement tool in the software was used for tracing Ca^{2+} activity on the regions of interest. The relative fluorescence change, $\Delta F/F$, was calculated from the time-lapse images of the G7NG817 mouse shown in Figures 4 and 5. F is the baseline value, which is the mean intensity of the 5 s period starting 10 s before tail pinching in Figure 4 and the 10 s period starting 30 s before tail inching in Figure 5; And ΔF is the difference from the baseline.
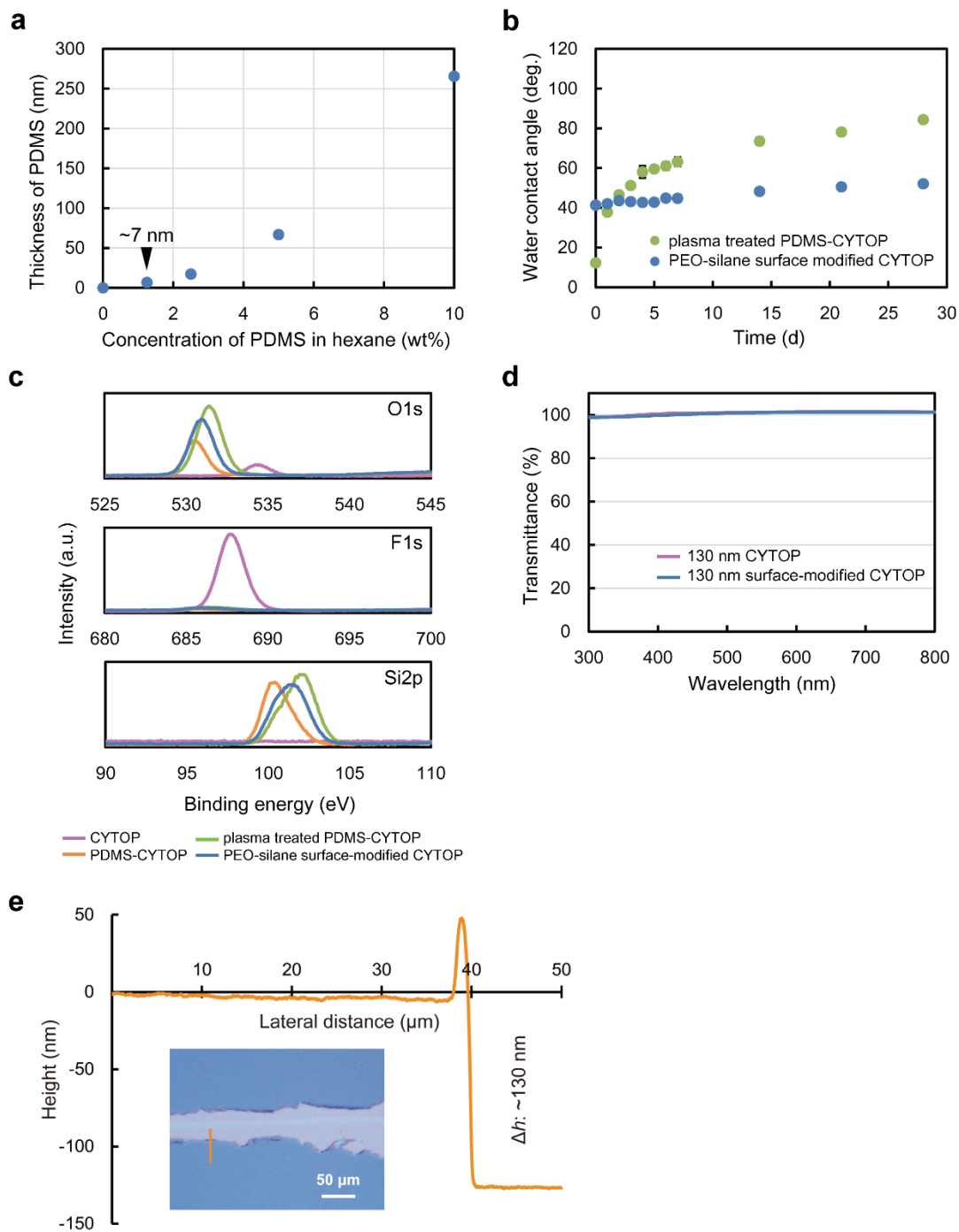
Figure **S1.** Supplementary results regarding the preparation and characterization
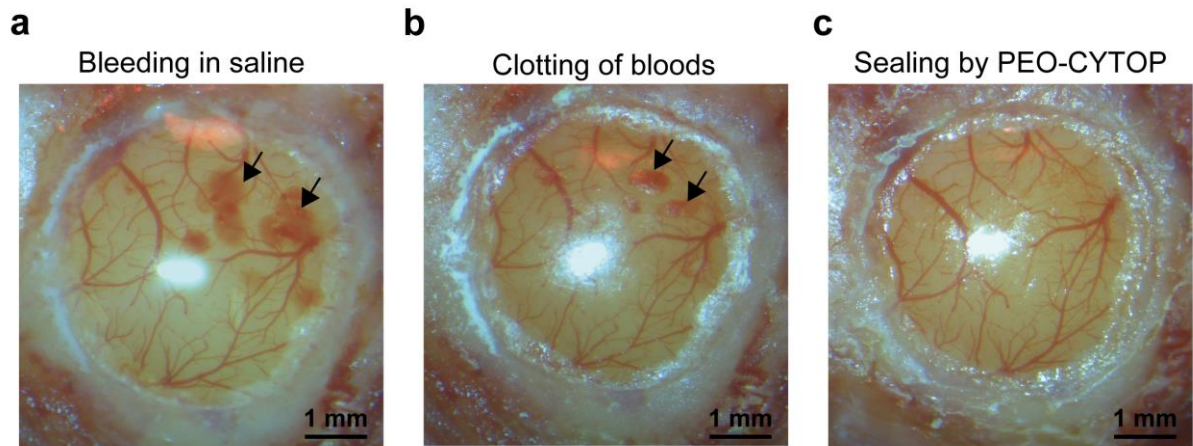
of PEO-CYTOP nanosheet. Related to Figure 1.

a, **The thickness of the** PDMS layer coated on the surface of the CYTOP

versus the concentration of PDMS in hexane for spin casting.

b, The static water contact angle of the plasma-treated PDMS-CYTOP nanosheet and the PEO-silane surface-modified CYTOP nanosheet during 1 month continuous observation.

c, X-ray photoelectron spectroscopy results of the surfaces of pristine CYTOP, PDMS-CYTOP, plasma-treated PDMS-CYTOP, and the PEO-silane surface-modified CYTOP nanosheet.

d, Transmittance in the wavelength from 300 to 800 nm of the CYTOP and PEO-CYTOP nanosheets with a similar thickness of ~130 nm.

e, Characterization of thickness using a stylus profilometer. Inset was the optical image of the scratching groove on the nanosheet made with a scalpel, and the orange line indicates the location of the moving stylus. The thickness of the nanosheet was determined from the average height difference between the surface of the nanosheet and the silicon wafer.
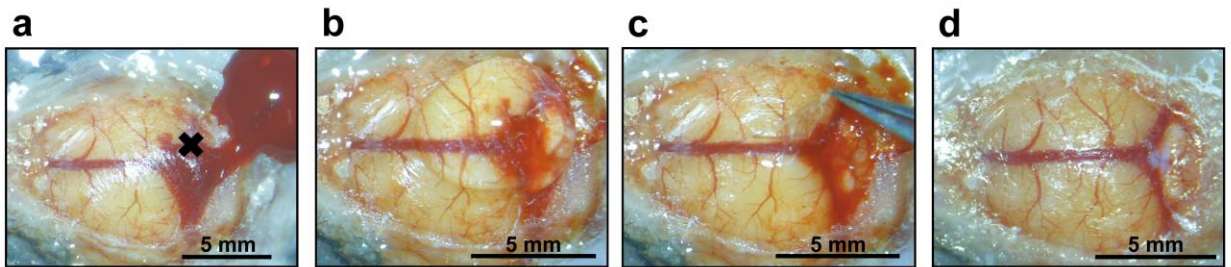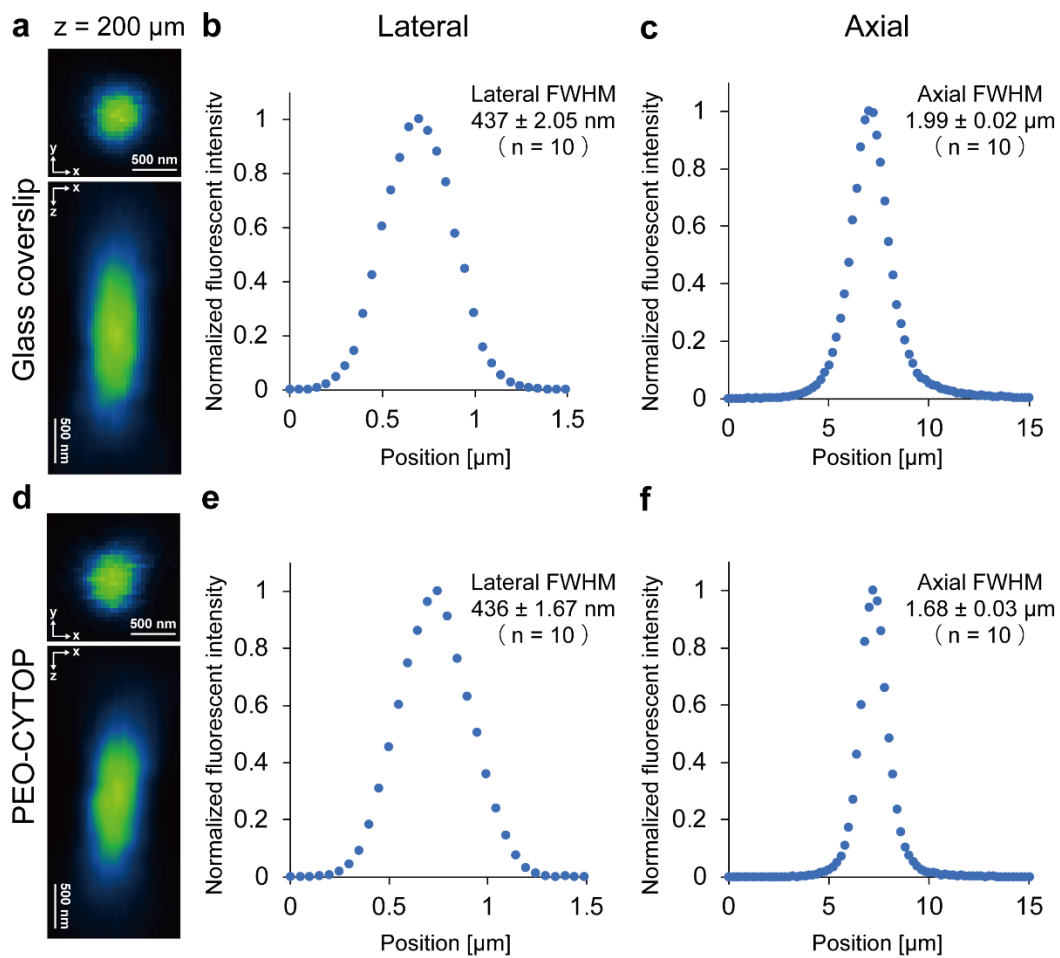
Figure S2. The procedure of the removal and resealing of the PEO-CYTOP nanosheet injuring right transverse sinus intentionally. Related to Figure 2.

a, Injuring the right transverse sinus by a needle intentionally. Black cross indicates the injured site.

b, Pouring saline into the broken PEO-CYTOP nanosheet to wash the blood from the injured site.

c, Removing the broken PEO-CYTOP nanosheet using tweezers.

d, Resealing the cranial window by another PEO-CYTOP nanosheet after washing the blood on the brain surface.

Figure S3. The suppression of bleeding and clotting of blood with PEO-CYTOP

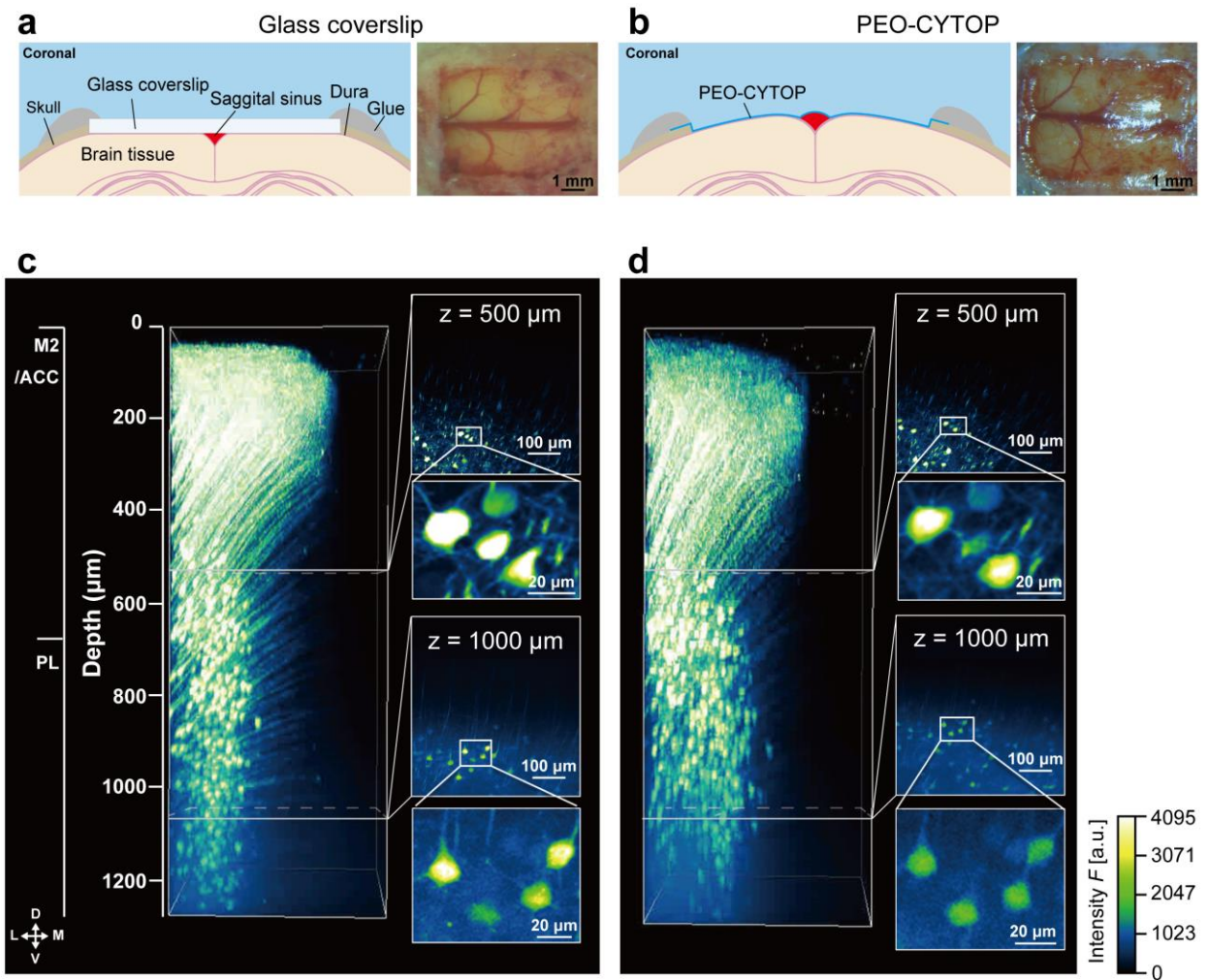nanosheet. Related to Figure 2.

a, Bleeding from the brain surface to saline after removing the skull. Arrows

indicate the bleeding sites.

b, The clotting of blood on the surface in the identical mouse of Figure S3a.

Arrows indicating the clotting sites.

c, The cranial window sealed by the PEO-CYTOP nanosheet in the identical

mouse of Figure S3a without bleeding and coagulation of blood after

washing the coagulation shown in Figure S3b.

a z = 200 μm   **b** Lateral   **c** Axial

Glass coverslip

Lateral FWHM
437 ± 2.05 nm
(n = 10)

Axial FWHM
1.99 ± 0.02 μm
(n = 10)

d   **e**   **f**

PEO-CYTOP

Lateral FWHM
436 ± 1.67 nm
(n = 10)

Axial FWHM
1.68 ± 0.03 μm
(n = 10)

Figure S4. Comparison of the axial and lateral resolution between PEO-CYTOP nanosheet and glass coverslip. Related to Figure 3.

a, Fluorescence images of 200-nm yellow-green beads using glass coverslip in xy (top) and xz (bottom).

b, Lateral normalized fluorescence intensity of 200-nm yellow-green beads using glass coverslip.

c, axial normalized fluorescence intensity of 200-nm yellow-green beads using glass coverslip.

d, Fluorescence images of 200-nm yellow-green beads using PEO-CYTOP in xy (top) and xz (bottom).

e, Lateral normalized fluorescent intensity of 200-nm yellow-green beads using PEO-CYTOP.

**f,** Axial normalized fluorescent intensity of 200-nm yellow-green beads using PEO-CYTOP.

Figure S5. *In vivo* two-photon imaging using the PEO-CYTOP nanosheet and a glass coverslip in turn. Related to Figure 3.

a, The cranial window sealed by a glass coverslip on the parietal cortex in the adult H-line mouse brain.

b, The cranial window sealed by PEO-CYTOP nanosheet on the parietal cortex in the adult H-line mouse brain.

c, Maximum intensity projections of the two-photon fluorescence images of PFC neurons with the glass coverslip. M2, Secondary motor cortex; ACC,

anterior cingulate cortex; PL, prelimbic cortex. The directions indicate dorsal

(D), ventral (V), medial (M), and lateral (L).

Maximum intensity projections of the two-photon fluorescence images of PFC

neurons of the mouse with the PEO-CYTOP nanosheet.
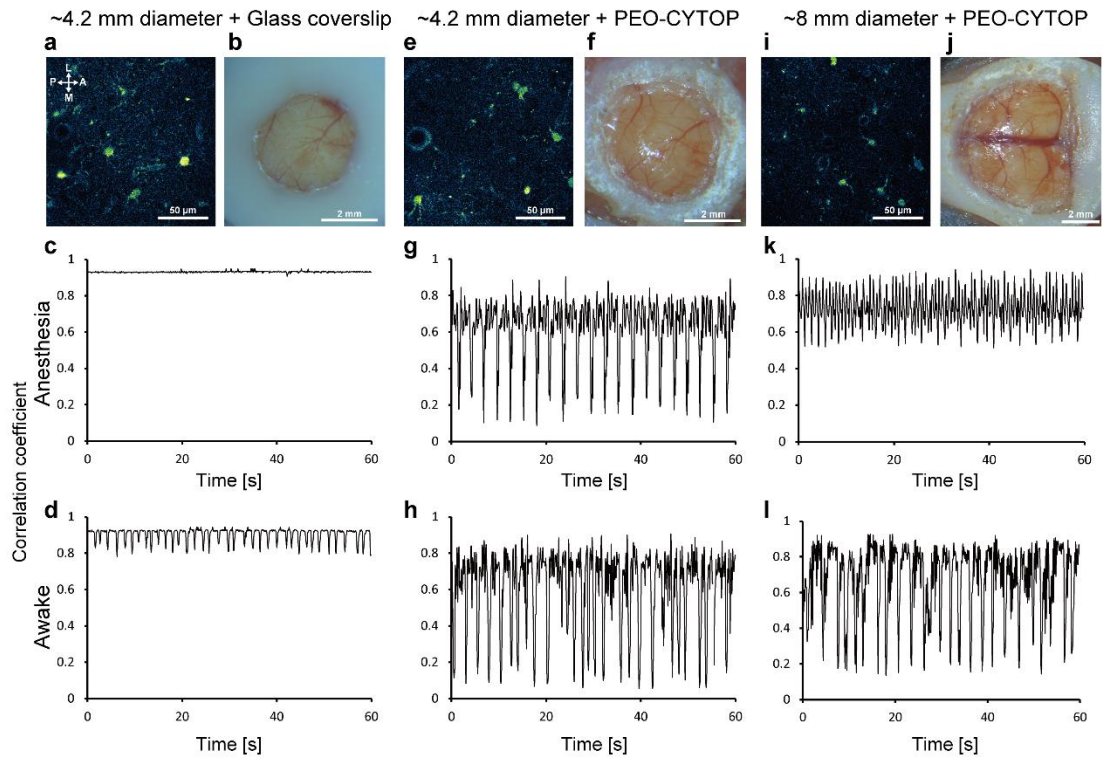
Figure S6. Evaluation of motion artifacts in anesthesia and awake mouse using both PEO-CYTOP nanosheet and a glass coverslip. Related to Figure 3.

a, An example image of two-photon imaging of astrocytes labeled with sulforhodamine 101 with small cranial window of glass coverslip. The directions indicate anterior (A), posterior (P), medial (M), and lateral (L).

b, A small cranial window sealed by glass coverslip on V1 area in the adult WT mouse brain.

c, Time series of correlation coefficient calculated from each frame in anesthesia condition of the mouse same as (a).

d, Time series of correlation coefficient calculated from each frame in awake condition of the mouse same as (a).

e, An example image of two-photon imaging of astrocytes labeled with sulforhodamine 101 with small cranial window of PEO-CYTOP nanosheet.

f, A small cranial window sealed by PEO-CYTOP nanosheet on V1 area in the adult WT mouse brain.

g, Time series of correlation coefficient calculated from each frame in anesthesia condition of the mouse same as (e).

h, Time series of correlation coefficient calculated from each frame in awake condition of the mouse same as (e).

i, An example image of two-photon imaging of astrocytes labeled with sulforhodamine 101 with large cranial window of PEO-CYTOP nanosheet.

j, Large cranial window sealed by PEO-CYTOP nanosheet on the parietal cortex in the adult WT mouse brain.

k, Time series of correlation coefficients calculated from each frame in the mouse under anesthesia same as (i).

l, The graph of time series of correlation coefficient calculated from each frame in awake condition of the mouse same as (i).

a Immediately after surgery

b 3d after surgery

1 mm

1 mm
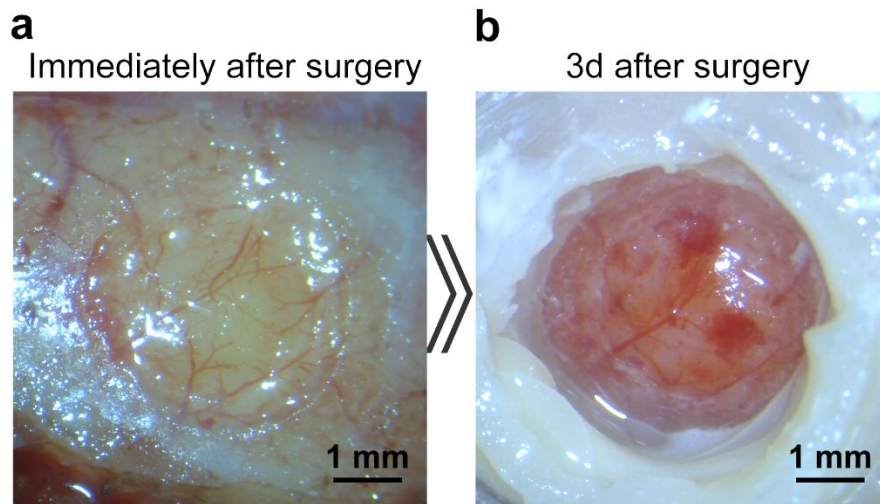
Figure S7. Examination of the brain tissue without any sealing materials. Related to Figure 5.

a, Image of the cranial window without any sealing material in a diameter of 3.5 mm.

b, Image of the cranial window shown in Figure S7a up to 3 days after surgery.
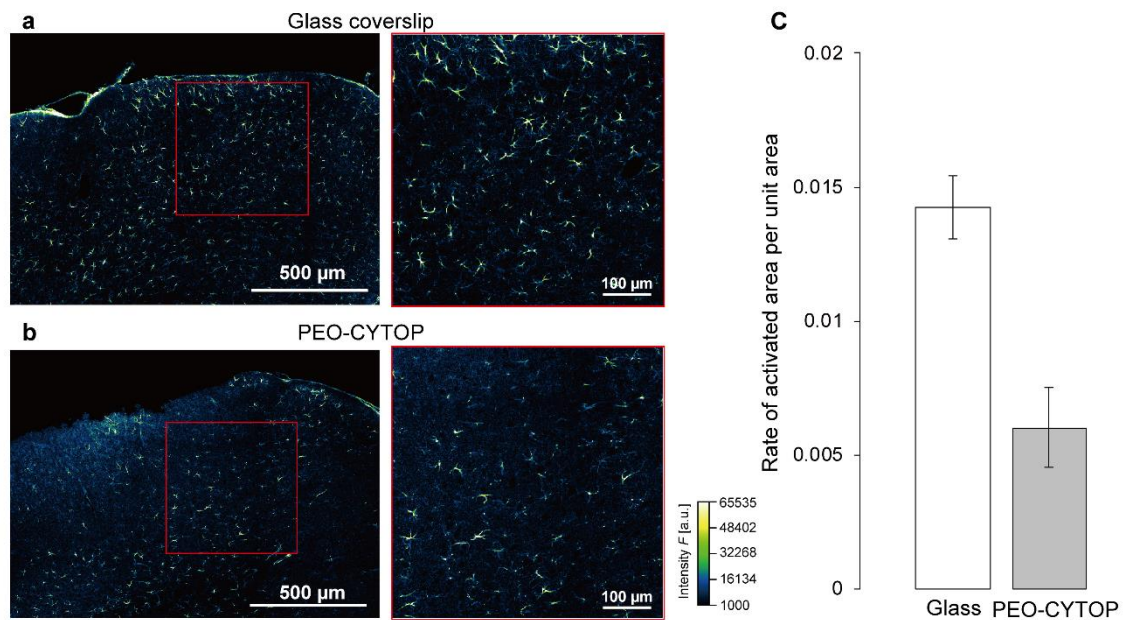
Figure S8. Immunostaining of GFAP in the brain tissue underneath cranial windows using each glass coverslip and PEO-CYTOP nanosheet. Related to Figure 5.

a, Immunostaining of anti-glial fibrillary acidic protein in a mouse of cranial window using glass coverslip 2 weeks after surgery.

b, Immunostaining image of anti-glial fibrillary acidic protein in a mouse of cranial window using PEO-CYTOP nanosheet 2 weeks after surgery.

c, Bar plots of the rate of the area of GFAP fluorescence per ~569 × ~569 μm^2 in both cases using glass coverslip and PEO-CYTOP. The activated areas